# Hydrodynamics of Meander Bends in Intertidal Mudflats: a Field Study From the Macrotidal Yangkou Coast, China

**Chao Gao[1,2], Alvise Finotello[2,*], Andrea D'Alpaos[2], Massimiliano Ghinassi[2], Luca Carniello[3], Yupeng Pan[1], Dezhi Chen[4], and Ya Ping Wang[1,5*]**

[1]*Ministry of Education Key Laboratory for Coast and Island Development, School of Geographic and Oceanographic Sciences, Nanjing University, Nanjing, 210093, China*

[2]*Dept. of Geosciences, University of Padova, via Gradenigo 6, IT-35131, Padova (Italy)*

[3]*Dept. of Civil, Environmental, and Architectural Engineering, University of Padova, via Marzolo 9, IT-35131, Padova (Italy)*

[4]*Key Laboratory of Tropical Marine Ecosystem and Bioresource, Fourth Institute of Oceanography, Ministry of Natural Resources, Beihai, 53600, China*

[5]*State Key Laboratory of Estuarine and Coastal Research, School of Marine Sciences, East China Normal University, Shanghai, 200062, China*

*Corresponding authors:

Ya Ping Wang (ypwang@nju.edu.cn );

Alvise Finotello (alvise.finotello@unipd.it)

## Key Points

- Acoustic measurements of flow velocities in a sinuous macrotidal mudflat channel show critical differences with channels in vegetated intertidal plains
- Offset between streamwise and cross-stream velocity maxima limits advection of secondary flows and hinders curvature-induced helical flows
- High velocities and sustained seepage flows at late-ebb stages likely exert stronger controls than helical flows on meander morphodynamics

## Keywords

Tidal Meanders; Mudflat; Hydroacoustic; Helical flow; Secondary circulations; Flow Separation

**Abstract**

Meandering channels are ubiquitous features in intertidal mudflats and play a key role in the eco-morphosedimentary evolution of such landscapes. However, the hydrodynamics and morphodynamic evolution of these channels are poorly known, and direct flow measurements are virtually nonexistent to date. Here, we present new hydroacoustic data collected synchronously at different sites along a mudflat meander located in the macrotidal Yangkou tidal flat (Jiangsu, China) over an 8-day period. The studied bend exhibits an overall dominance of flood flows, with velocity surges of about 0.8 m/s occurring immediately below the bankfull stage during both ebb and flood tides. Unlike salt-marsh channels, velocities attain nearly-constant, sustained values as long as tidal flows remain confined within the channel, and reduce significantly during overbank stages. In contrast, curvature-induced cross-sectional flows are more pronounced during overbank stages. Thus, a phase lag exists between streamwise and cross-stream velocity maxima, which limits the transfer of secondary flows and likely hinders the formation of curvature-induced helical flows along the entire meander length. Our results support earlier suggestions that the morphodynamics of intertidal mudflat meanders does not strongly depend on curvature-induced helical flows, and is most likely driven by high velocities and sustains seepage flows at late-ebb stages, as well as by other non-tidal processes such as waves and intense rainfall events. By unraveling complex flow structures and intertwined morphodynamic processes, our results provide the first step toward a better understanding of intertidal mudflat meanders, with relevant implications for their planform characteristics and dynamic evolution.

## 1 Introduction

Tidal mudflats are among the most extensive coastal ecosystems worldwide (Murray et al., 2019; Murray et al., 2022). They are low-gradient intertidal landforms typically occurring in sediment-rich environments (Gao, 2019; Klein, 1985; Rogers & Woodroffe, 2015) characterized by large tidal oscillations relative to characteristic wind-wave heights (e.g., Friedrichs, 2011; Klein, 1985; Morales, 2022). Tidal mudflats are extremely important from both ecological and economic perspectives thanks to the broad range of ecosystem services they provide (Passarelli et al., 2018), including, nutrient cycling, carbon sequestration, water filtering, habitat provision for wildlife, food production, recreational activities, and cultural services (Choi, 2014; Friedrichs & Perry, 2001; Kim et al., 2000; Kirwan & Megonigal, 2013; Pilkey & Cooper, 2004; Shi et al., 2018; Temmerman et al., 2013; Vousdoukas et al., 2020; Wang et al., 2012).

The morphosedimentary evolution of tidal mudflats is intimately linked to the morphodynamics of the extensive networks of tidal channels that cut through them (Figure 1). These channels are typically meandering in planform to a greater or lesser degree (Choi, 2014; Friedrichs, 2011; Gao, 2019; Hughes, 2012), and play a primary role in regulating the exchanges of water, sediments, nutrients, and biota with the open sea (Coco et al., 2013; D'Alpaos et al., 2005), thus exerting a prominent control on the eco-geomorphology of the tidal-flat ecosystem as a whole (Choi, 2014; Hughes, 2012; Wells et al., 1990). Besides, lateral migration of meandering channels critically affects both the sedimentology and stratigraphy of tidal-flat systems, especially in terms of preservation potential (Choi, 2011; Choi et al., 2013; Ghinassi et al., 2019; Kleinhans et al., 2009). Indeed, mudflat tidal channels are typically preserved in the fossil record either as laterally-accreting, heterolithic point bars or through the infilling of abandoned channels generated either from meander cutoff or channel avulsion (Brivio et al., 2016; Choi, 2010; Cosma et al., 2020; Hughes, 2012; Sisulak & Dashtgard, 2012).

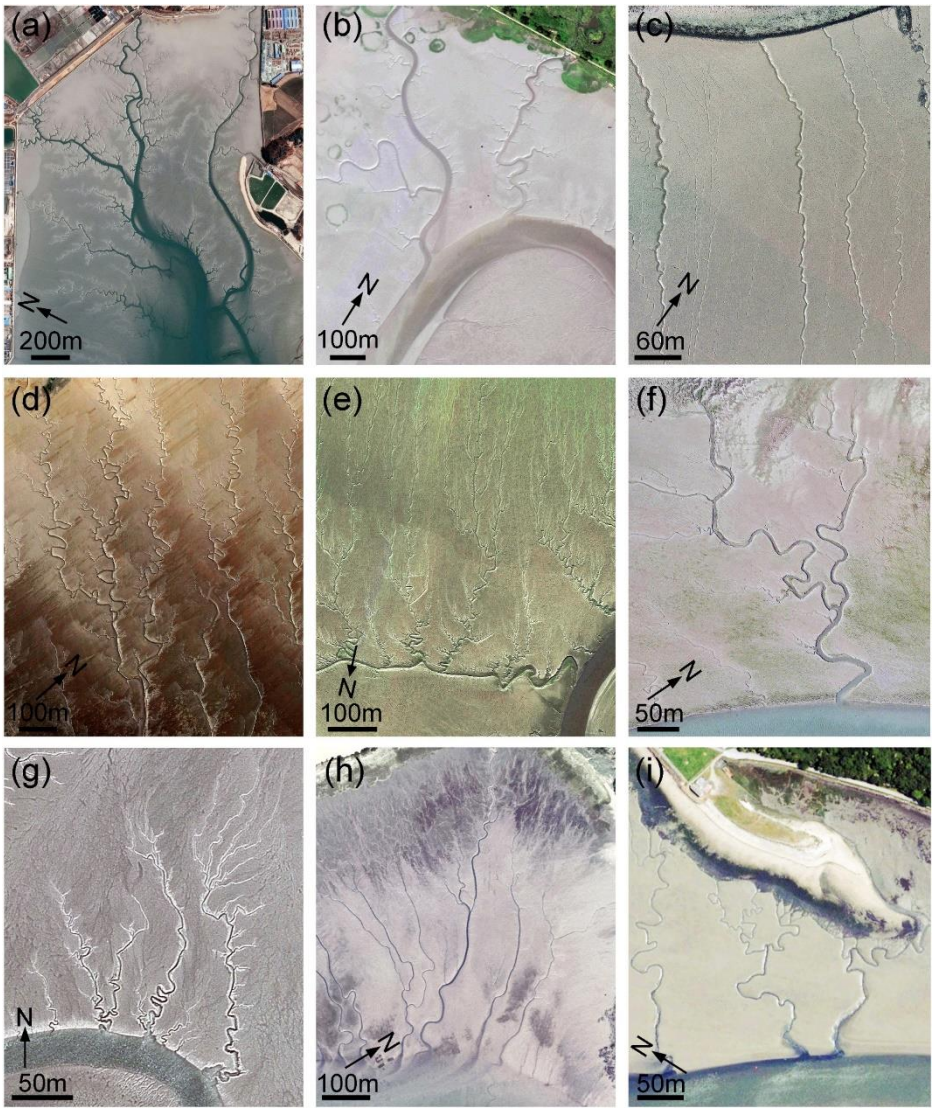


Figure1. Examples of meandering channels in tidal mudflats along the World's coast. (a) Baegmihang Port, South Korea (37°09′N, 126°40′E; ©Google, TerraMetrics; imagery date: March 14, 2019). (b) Boseong Bay, South Korea (34°52′N, 127°30′E; ©Google, Maxar Technologies; imagery date: August 30, 2020). (c) Cardiff Flats, England (51°28′N, 3°08′W; ©Google, Maxar Technologies; imagery date: July 11, 2013). (d) Fundy Bay, Canada (45°45′N, 64°38′E; ©Google, Maxar Technologies; imagery date: May 21, 2017). (e) Mühlenberger Loch, Germany (53°32′N, 9°48′E; ©Google, CNES/Airbus; imagery date: April 22, 2020). (f) The Wadden Sea, Germany (53°41′N, 8°02′E; ©Google, Maxar Technologies; imagery date: September 25, 2016). (g) I'Épinay Estuary, France (47°31′N, 2°36′W; ©Google, Maxar Technologies; imagery date: March 19, 2011). (h) Lanveur Bay, France (48°21′N, 4°17′W; ©Google, Landsat/Copernicus; imagery date: January 01, 2005). (i) Morlaix Bay, France (48°38′N, 3°51'W; ©Google, TerraMetrics; imagery date: January 01, 2005).

In spite of their prominence and ubiquity, however, meandering channels in tidal mudflats are still poorly studied especially from a hydrodynamic standpoint. Previous field measurements of flow fields in tidal meanders focused primarily on either tidally-influenced fluvial reaches, where flow dynamics are largely influenced by river discharges and density-stratification effects (Chant, 2002; Keevil et al., 2015; Kranenburg et al., 2019; Somsook et al., 2020), or on intertidal channels dissecting vegetated salt marshes and mangrove swamps (Finotello, Ghinassi, et al., 2020; Horstman et al., 2021). In contrast, field studies on tidal meanders wandering through unvegetated intertidal mudflats are still scarce (Choi et al., 2013; Kleinhans et al., 2009), and flow velocity measurements are virtually nonexistent to date. This is a critical knowledge gap because significant differences might exist in terms of flow fields between tidal channels wandering through vegetated and unvegetated intertidal plains, especially concerning overbank stages (i.e., water levels that exceed the channel bankfull capacity). Overbank velocities in vegetated settings dominated by turbulence and friction are typically a magnitude lower than those observed on unvegetated mudflats (Bouma et al., 2005; Christiansen et al., 2000; D'Alpaos et al., 2021; Friedrichs, 2011; Hughes, 2012; Rinaldo et al., 1999a; Sullivan et al., 2015). Besides, overbank stages are more frequent in mudflats than in salt marshes, owing to the relatively lower position occupied by mudflat channel banks within the intertidal frame. As such, stage-velocity relations in mudflat tidal channels can differ greatly from those observed in vegetated marshes and mangrove forests, and overbank stages might have stronger control on tidal channel morphodynamics (D'Alpaos et al., 2021; Hughes, 2012; Kearney et al., 2017; McLachlan et al., 2020; Sgarabotto et al., 2021), potentially justifying the observed morphological differences of tidal channel networks in distinct vegetational settings (Geng et al., 2021; Kearney & Fagherazzi, 2016; Schwarz et al., 2022; Wang et al., 1999a, 1999b). These differences in landforming hydrodynamic processes are also likely to affect the development of curvature-induced helical flow that is typically related to the development and growth of meander bends in both rivers and salt-marsh tidal channels (Azpiroz-Zabala et al., 2017; Finotello, Ghinassi, et al., 2020; Keevil et al., 2015; Kranenburg et al., 2019; Nidzieko et al., 2009; Thorne et al., 1985). Such helical flow forms as a consequence of secondary (i.e., cross-sectional) circulations, oriented toward the inner and outer bank in the near-bed and near-surface zone, respectively, which result from the imbalance between the upward-increasing centrifugal forces and the lateral pressure gradients created by the curvature-induced superelevation of the water surface at the outer bank (Engelund, 1974; Prandtl, 1926; Rozovskiĭ,

1957; Solari et al., 2002). The downstream advection of secondary circulations operated by the main streamwise flow produces a helical flow, as extensively documented in a variety of field (Dietrich & Smith, 1983; Dinehart & Burau, 2005; Frothingham & Rhoads, 2003), laboratory (Blanckaert, 2011; Liaghat et al., 2014), and numerical studies (Blanckaert & de Vriend, 2003; Bridge & Jarvis, 1982; Ferguson et al., 2003).

Although secondary currents akin to those found in river meanders have been observed and modelled in meandering salt-marsh creeks and large estuarine tidal channels (Finotello, Canestrelli, et al., 2019; Finotello et al., 2022; Finotello, Ghinassi, et al., 2020; Kranenburg et al., 2019; Nidzieko et al., 2009; Pein et al., 2018; Somsook et al., 2020; Somsook et al., 2022), their presence in sinuous mudflat channels has yet to be demonstrated. In fact, previous studies (e.g., Choi, 2011; Choi & Jo, 2015; Ghinassi et al., 2019; Kranenburg et al., 2019) suggested that the morphodynamic processes governing meander evolution in intertidal mudflat settings can differ greatly from the classic secondary-current-driven lateral channel migration mechanism acting in vegetated fluvial and intertidal plains. For instance, Kleinhans et al. (2009) argued that owing to the higher thresholds for erosion that characterize mudflat deposits, bank erosion is primarily due to bank undercutting caused by backward-migrating steps along the channel bed driven by hydraulic jumps that form during ebb tides. They also demonstrated that bank migration occurs preferentially in very sharp bends, where flow separates from the meander inner (convex) bank and impinges directly against the outer (concave) bank. Choi (2011) noted enhanced tidal channel migration in association with episodic and seasonal increase of discharge due to, for example, heavy precipitations, pointing to a strong control of these non-tidal processes on the morphodynamic and sedimentology of tidal mudflat meanders. Accordingly, Choi and Jo (2015) measured pronounced meander migration in the Yeochari macrotidal flat (South Korea) during the summer rainy season, when point bars were observed to migrate as fast as 40 m per month due to increased runoff discharge caused by heavy rainfalls in the order of tens to hundreds of millimeters per hour, possibly compounded by monsoon precipitations. Finally, Ghinassi et al. (2019) suggested that wave winnowing of mudflats during high-tides modulates meander morphosedimentary evolution, leading to widespread bank collapses within the channel.

In view of the above, the structure of tidal flow fields in mudflat tidal meanders appears to be worth investigating. Here we present novel hydroacoustic data from a meandering tidal channel

dissecting a macrotidal mudflat located along the Jiangsu coast (China). The aim of the study is threefold, as we intend to: (i) highlight the characteristics of tidal flows within a meander bend developed in an unvegetated tidal mudflat; (ii) unravel possible differences in meander hydrodynamics among below-bankfull and above-bankfull (i.e., overbank) water stages; and (iii) disclose the characteristics of secondary circulations and their relations with the overbank flows. To the best of our knowledge, this study represents the very first attempt to directly measure tidal flows in meandering mudflat channels.

## 2 Geomorphological setting and study-case

Our study case is found in the Yangkou tidal flat (YTF), an extensive mudflat system located on the southern Jiangsu coast, northward of the Yangtze River Delta, which is bordered by the Yellow Sea to the East and North and by the East China Sea to the South (Figure 2a). The YTF was formed by abundant sediment supply input from both the Yangtze River and the Yellow River, which historically allowed for seaward expansion of the whole Jiangsu province coastline (Shi et al., 2016; Wang & Zhu, 1990). Sediments consist mainly of silty-muddy material, with average grain sizes ranging between 10 and 45 μm (i.e., 4.5 ~ 6.6 φ) (Shi et al., 2016; Wang & Ke, 1997). In the last 2 centuries, however, the seaward extent of the YTF has decreased from 5 ~ 11 km to about 5 ~ 8 km as a consequence of changes in sediment transport regime driven by anthropogenic interventions, the latter including the diversion of the Yellow River to the Bohai Sea in 1855 (Ren & Shi, 1986), and the construction of the Three Gorges Dam in 2003, which significantly decreased sediment supply from the Yangtze River (Yang et al., 2014). In addition to this, land reclamation projects, the building of oceanic outfalls, aquaculture, and the construction of wind farms have further contributed to increasing anthropogenic pressures in the YTF area (Xu et al., 2019; Zhao et al., 2020; Zhao & Gao, 2015). Nowadays, the whole intertidal area in the YTF covers approximately 100 $km^2$, extending seaward from the shoreline with gentle slopes ranging between 0.5‰ and 1.2‰ on average (Wang & Ke, 1997; Zhu et al., 1986).

Intertidal mudflats in the YTF are dissected by extensive networks of tidal channels. These channels serve as the main conduits for the propagation of both the East China Sea progressive tidal wave and the southern Yellow Sea rotary tidal wave, which converge nearby the town of

Yangkou giving rise to complex coastal circulations (Liu et al., 1989). The tidal regime in the study area is semidiurnal macro-tidal, with average and spring tidal ranges equal to 4.6 m and 8 m, respectively. Morphodynamic processes are also affected by the East Asian Monsoon, which blows with a mean winter wind speed of 4.2 m/s toward the southeast and a mean summer wind speed of 2.8 m/s toward the northwest, respectively (maximum measured wind speed is 34 m/s; (Li et al., 2011; Xing et al., 2012). As wave conditions in this region are mainly related to wind speeds, wave heights are smaller in the summer and larger in the winter, with annual average values ranging between 0.5 and 1.5 m (Chen, 2016). The annual precipitation is about 900 ~ 1000 mm on average, with the summer season accounting for more than 40% of the whole yearly rainfall (Wang & Ke, 1997; Xing et al., 2012).

Our study site is a blind tidal channel found within a natural reserve facing the Xiaoyaokou Scenic and the Xinchuan port, both located nearby the city of Yangkou (Figure 2b). The studied channel is 1.9 km long and is characterized by average width of 8 m. With an overall channel sinuosity equal to 1.5, it represents a well-developed meandering reach. The channel originates from a fringing salt marsh, which borders the Xiaoyangkou Scenic and is covered by *Spartina alterniflora Loisel* (Figure 2c,e), and extends seaward wandering through an unvegetated intertidal mudflat. Freshwater fluxes from the Beiling river to the North and the Bencha canal to the South do not interfere with the hydrodynamic regime of the studied channel, which is always submerged at high tide and drains out almost completely at low tide.

In this study, we focused specifically on a meander bend located in the central portion of the channel and surrounded by unvegetated tidal flats (Figure 2c,d,f). The studied bend is characterized by a cartesian wavelength (i.e., the linear distance between bend inflections) $L_{xy}$=37 m, whereas the along-channel bend length ($L_s$) is equal to 56 m. Hence, the bend attains a sinuosity $\chi$=$L_s/L_{xy}$=1.5. The average meander radius of curvature is $R$=19 m, and the amplitude, measured as the maximum distance from the line passing through both bend inflections, is equal to $A$=18 m. The cross-sectional width ($W$) decreases from 8.8 m to 8.3 m in the landward direction (average width $\overline{W}$=8.5 m). Being the bankfull depth ($Y_B$) equal 1.20 m on average, the studied bend is characterized by an average width-to-depth ratio ($\beta = \overline{W}/Y_B$) of about 7.1. All these morphometric parameters are in line with typical values observed for tidal channels worldwide (D'Alpaos et al., 2005; Finotello, D'Alpaos, et al., 2020; Hughes, 2012). While many regularly-

spaced small erosional gullies cut through the channel banks (Figure 2f), a 4 m wide and 0.5 m deep side tributary, meandering in planform, is found landward of the apex of the studied bend (Figure 2d).

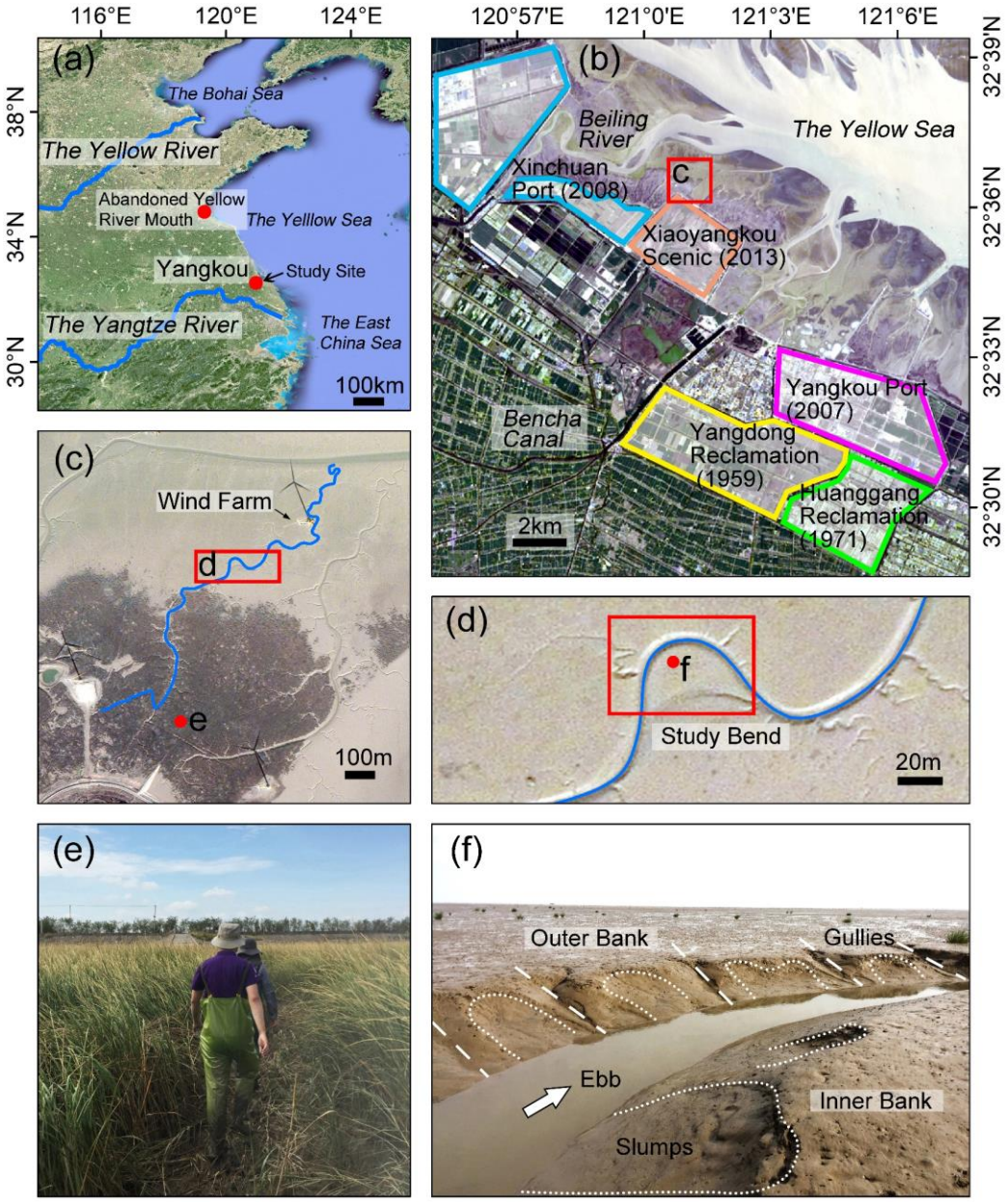


Figure 2. Study site. (a) Overview of the study area. (b) The Yangkou tidal flat, Rudong County, Jiangsu Province, China (Map data: Landsat8, OLI, April 9, 2021); areas affected by land reclamation activities are highlighted with colored lines. (c, d) Overview of the meandering tidal channel investigated in this study, with a close-up view of the analyzed meander bend (Map data: Google, TerraMetrics). (e) A photo showing vegetation features in the landward portion of the channel, characterized by the widespread presence of *Spartina alterniflora Loisel*. (f) A photo of the studied bend at low tide.

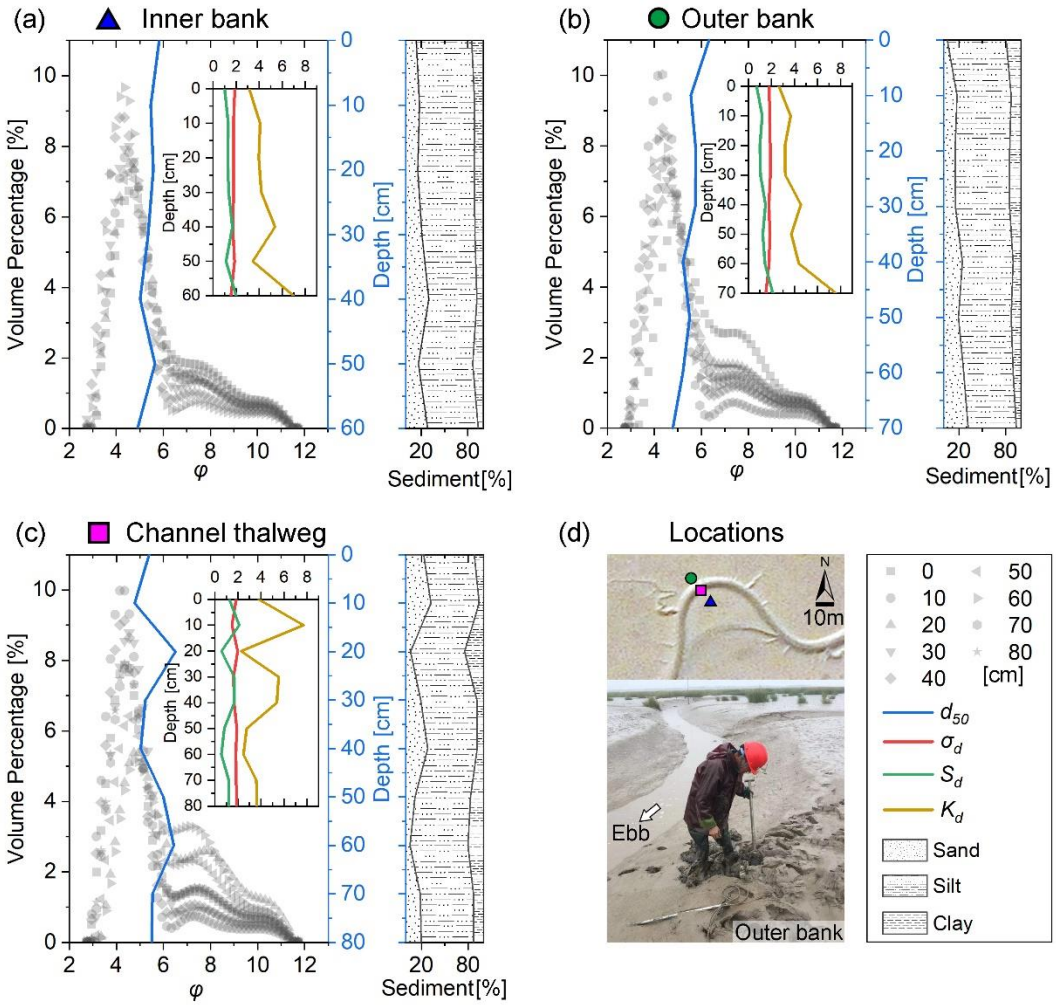


Figure 3. Sediment grain size distribution at the study site. Results of grain size analysis carried out on sediment cores collected at the study-bend inner bank (a), outer bank (b), and channel thalweg (c). Different symbols of gray-shaded data points denote different coring depths, as shown by the inset in the lower-right corner. Detailed coring locations are shown in panel (d), together with a seaward-looking photo of the coring operation at the outer bank. Sediment coring was carried out on the last day of fieldwork to avoid damaging the channel morphology before flow measurements.

In order to investigate sediment properties at the study site, we collected sediment cores at the meander inner bank, outer bank, and channel thalweg using a custom hand corer (coring depth ranging between 60 and 80 cm). Grain-size analysis was carried out at 10 cm intervals from the core top using a Mastersizer 2000 laser granulometer with a measuring range of 0.02 ~ 2000 μm

and a reproducibility error of < 3%. Grain-size parameters - including median size ($d_{50}$), standard deviation ($\sigma_d$), skewness ($S_d$), and kurtosis ($K_d$) - were calculated using the Moment Methods (Friedman, 1962). Consistently with sedimentary characteristics of the whole YTF system, sediments were found to be mostly cohesive, with clay volume content accounting for nearly 20% (Figure 3). The median grain size is always smaller than 62.5 μm (i.e., 4φ). No significant grain-size trends are observed from the core collected at the channel thalweg (Figure 3c), whereas fining upward trends are found both at the inner and outer bank (Figure 3a,b).

## 3 Methods

### 3.1 Acoustic measurements of flow velocities

We continuously monitored water levels and flow velocities in the study meander bend from October 14, 2020 to October 21, 2020. Three Nortek's new Acoustic Doppler Current Profiler (AD2CP, Signature 1000kHz) were placed at three different sites along the studied bend, namely the bend apex and both the landward and seaward inflections, whereas one Teledyne RDI ADCP1200kHz was deployed at the confluence with the small side tributary (Figure 4a). All instruments were placed at the channel thalweg with an up-looking orientation to record velocities and pressures (Figure 4c,d,e,f). The fifth probe of Nortek AD2CPs can observe the vertical velocity separately from the other four probes, thus effectively avoiding acoustic cross-interference so that the noise in the vertical velocity signal is significantly lower than that of traditional ADCP instruments. The three AD2CPs were programmed to operate at 1.0 Hz, recording velocities in 20 cm vertical bins over timespans at 5-minute intervals. The blanking distance of the AD2CP was set to 10 cm, so that the center of the first sampling bin is 20 cm above the instrument. In contrast, the Teledyne ADCP was programmed to operate at 1.0 Hz to record velocities in 5 cm bins at 5 minutes. The blank distance of the ADCP was set to 20 cm, so that the center of the first bin is 22.5 cm above the instrument. Details regarding the instruments' parameters are shown in Table 1.

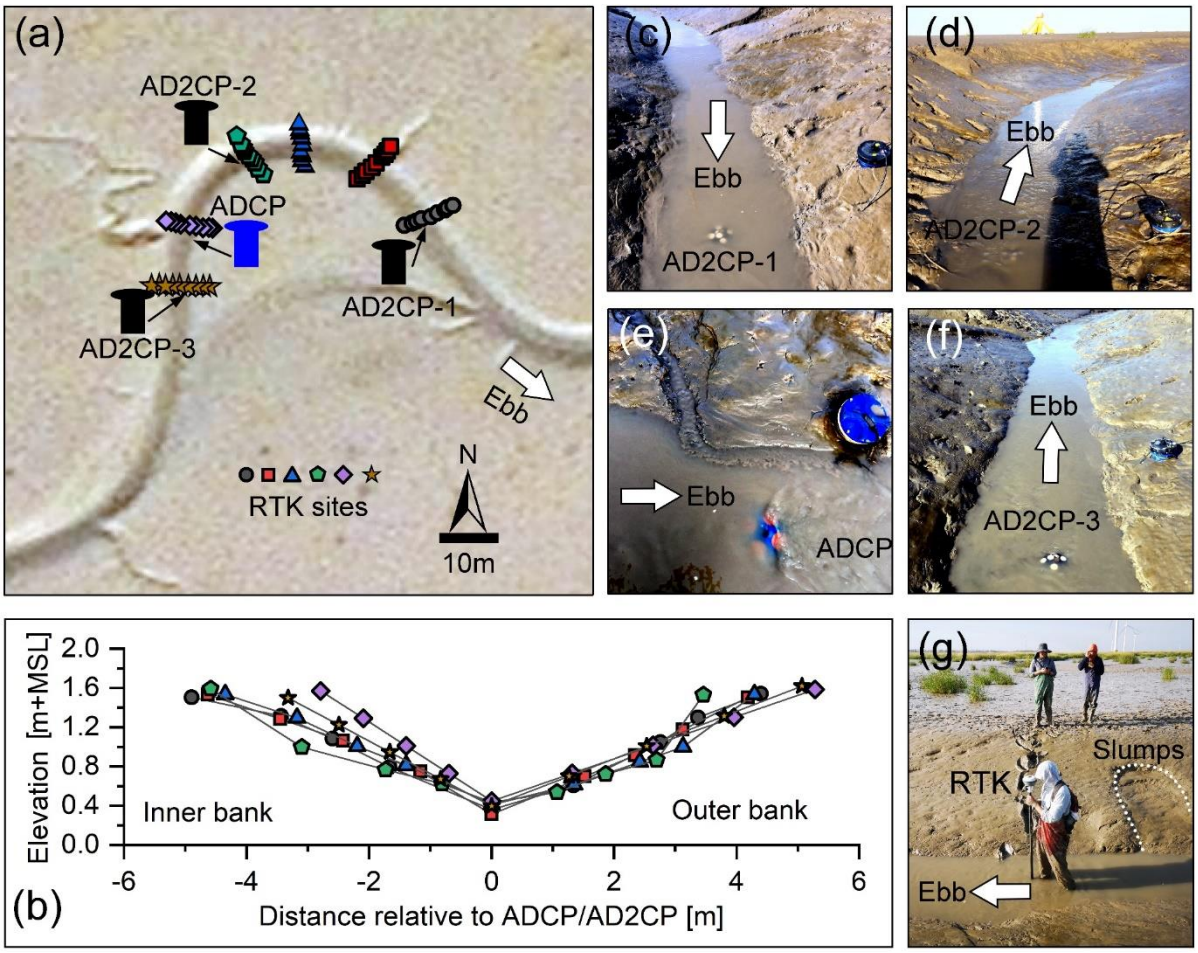


Figure 4. Field measurements of flow fields and channel geometry. (a) Deployment locations of the AD2CPs (in black) and ADCP (in blue) instruments used in this study are shown together with the channel cross-sections where topographic surveys were carried out by means of an RTK-GPS. (b) Cross-sectional profiles of the surveyed channel cross-sections as obtained from the RTK data. Elevations are reported in meters above the mean sea level (MSL). Different symbols and colors denote different cross-sections according to the legend shown in panel "a". (c,d,e,f) Photograph of the deployed instrument prior to data acquisition. Names of individual instruments recall those reported in panel "a". (g) Photo of the topographic survey campaign carried out by means of an RTK-GPS during low tide. All the photos reported in panels (c,d,e,f, and g) were taken during the late stages of ebb tides.

280 Table 1. Parameters of the AD2CP and ADCP instruments used in this study

| | AD2CP-1 | AD2CP-2 | AD2CP-3 | ADCP |
|---|---|---|---|---|
| Manufacture | Nortek | Nortek | Nortek | Teledyne RDI |
| Version | Signature1000 | Signature1000 | Signature1000 | Workhorse |
| Serial Number | 100295 | 101044 | 100615 | |
| Sampling rate | 1 Hz | 1 Hz | 1 Hz | 1 Hz |
| Blanking Distance | 10 cm | 10 cm | 10 cm | 20 cm |
| Bin Size | 20 cm | 20 cm | 20 cm | 5 cm |
| Sampling Mode | Burst | Burst | Burst | Burst |
| Sampling Interval | 5 min | 5 min | 5 min | 5 min |
| Sample Duration | 256 s | 256 s | 256 s | 256 s |
| Burst Profile | 5 Beams | 5 Beams | 5 Beams | 4 Beams |

281

282 **3.2 Data processing**

283 Velocity data retrieved from the AD2CPs were converted into ENU system (i.e., $v_E$, $v_N$,$v_U$ for
284 East-, North-, and Up-ward velocity, respectively), whereas ADCP data were already recorded in
285 ENU format. Raw ENU data were then imported to Matlab (version 2019b) for initial quality
286 control to remove noise generated by the interference of water bubbles, large suspended particles,
287 echo intensity, and other disturbance factors (Lan et al., 2019). The procedure used for quality
288 control is a modified version of Guerra and Thomson (2017)'s algorithm. For the data acquired
289 using AD2CPs, values of echo intensity ≥ 25 dB and correlation magnitude ≥ 30% are used as
290 threshold limits for high-quality data; for the data acquired by ADCP, values of echo intensity ≥
291 30 dB and correlation magnitude ≥ 50% are instead used as thresholds. Velocity data were then
292 despiked using the Phase-Space Thresholding Method (Goring & Nikora, 2002) and eventually
293 averaged over the time length of individual bursts (i.e., 5 minutes). Moreover, ADCP data were
294 also averaged vertically over 4 successive bins to allow for a more direct comparison with the
295 AD2CP data. Overall, a total of 21 bins of velocity data were obtained for each instrument. For
296 each bin, the horizontal velocity $\vec{v}$ was calculated as the vector sum of the eastward ($\overrightarrow{v_E}$) and
297 northward ($\overrightarrow{v_N}$) velocity components (see Figure 5a) whereas depth-averaged velocities (*DAVs*)
298 were computed for each measuring station as the average value of the whole $\vec{v}$ profile. Measured

values of upward velocities ($\overrightarrow{v_U}$) were instead maintained unaltered. Water depth ($Y$) data were also obtained from pressure sensors integrated within the instruments. Based on the surveyed topographic profile of each cross-section (Figure 4b), we were able to identify the water depth $Y_B$ corresponding to bankfull conditions. This allowed us to differentiate velocity data recorded for water levels higher and lower than the bankfull threshold (i.e., above- and below-bankfull water stages). Stage-velocity diagrams were also obtained based on binary plots of water levels ($Y$) and depth-averaged values of flow velocity ($DAVs$) at each monitoring station (Figure 6 a-d). Both $DAVs$ and $Y$ were also put in relation to the rates water-level change $\dot{Y} = dY/dt$ (Figure 6 e-p).

Tidal asymmetries were investigated based on two distinct metrics, concerning the asymmetry in flood vs. ebb peak tidal velocities and flood vs. ebb durations, respectively (Figure 5 e-g). Since the flow velocity is a function of the water depth, the peak tidal velocity index ($\rho_v$), which is the ratio between the flood and ebb peak of $|\vec{v}|$ (Friedrichs & Aubrey, 1988; Guo et al., 2019), was calculated at different water depths (i.e., at different positions along the water column) at 20 cm intervals. To further differentiate between flow dynamics within the channel and outside of it, distinct calculations of $\rho_v$ were performed averaging results by considering only velocity values measured at water depths ($Y$) smaller and larger than the bankfull depth ($Y_B$), respectively (Figure 5e,f). In contrast, asymmetries in tidal duration ($\rho_d$) were computed as the ratio between the duration of the falling and rising limb of the tidal wave (Friedrichs & Aubrey, 1988; Guo et al., 2019). Both $\rho_d$ and $\rho_v$ provide a straightforward tool to differentiating flood-dominated ($\rho$>1) and ebb-dominated ($\rho$<1) tidal flows.

To simplify the interpretation of velocity-data time series and filter out outliers, data were phase averaged and subdivided into two distinct groups based on the values of the high-tide water depth ($Y_H$) observed during each individual tidal cycle. Specifically, tidal cycles for which $Y_H$>3.7 m (i.e., the sixth to thirteenth tidal cycle in Figure 5) were classified as "high-amplitude tides" (*HAT*), whereas all the other tidal cycles were considered "low amplitude tides" (*LAT*) (Tu et al., 2019; Voulgaris & Meyers, 2004; Wang et al., 2013). For each tidal cycle, the instant corresponding to $Y_H$ was assigned the time value of $t$=0. Then, data collected six hours before and after $Y_H$ were ensemble-averaged at five-minute intervals (Figure 7a,b)

Finally, in order to better investigate flow structures and unravel possible secondary (i.e., cross-sectional) circulations, velocity data were reprojected into two different components, namely, the

primary (i.e., streamwise) velocity $V_P$, corresponding to the main direction of in-channel tidal flows, and the secondary (i.e., cross-sectional) velocity $V_S$, oriented orthogonally to $V_P$ (Bever & MacWilliams, 2016; Finotello, Ghinassi, et al., 2020; Lane et al., 2000). In order to define the directions of $V_P$ and $V_S$, previous studies have typically taken advantage of reprojection techniques based on flow data recorded along the entire channel cross-section by ADCP instruments mounted on moving vessels (Finotello, Ghinassi, et al., 2020; Lane et al., 2000; Parsons et al., 2013). These techniques cannot however be applied to our data, since our instruments were operated in stationary mode, and significant differences appear when observing flow velocities at above- and below-bankfull stages. Thus, we assumed that the direction of $V_P$ corresponds to the direction of the maximum horizontal velocity ($\overrightarrow{v_{max}}$) observed at the bottom vertical layer (i.e., $Y$ = 0.2 m in Figure 7c~f). Such a definition is based on the observation that the orientation of $\overrightarrow{v_{max}}$ at the channel bottom is unequivocally defined and remains consistent during both the ebb and flood phases (see Figure 4 and Figure 7c~f). Once $V_P$ is defined, the orientation of secondary velocity ($V_S$) is immediately derived as the direction perpendicular to $V_P$. Details regarding the determination of $V_P$ and $V_S$ at different measuring stations can be seen in Figure 8,9,10 and 11. Close-up views of $V_S$ vectors for below-bankfull stages only are also shown in Supplementary Figure S1.

## 4 Results

### 4.1 Flow magnitudes, tidal asymmetries, and stage-velocity relationships

Overbank flows invariably occurred for all the tide cycles on record. The high-tide water depth ($Y_H$) reached a maximum value of 4.2 m on Oct. 18, whereas a minimum value of $Y_H$=2.2 m was observed on Oct. 14. The latter was still higher than bankfull water depth ($Y_B$), which is about $Y_B$=1.20 m (Figure 5a). There are no significant differences in horizontal velocity magnitudes ($|\vec{v}|$) between the four monitoring stations, with peak velocities in the order of $|\vec{v}|$=0.96-0.99 m/s consistently observed during the rising limb of the tide (Figure 5a,b,c,d). Pronounced differences in flow velocity are observed for water stages above and below the bankfull depth. Specifically, higher $|\vec{v}|$ values are typically observed for below-bankfull water stages, when tidal flows are conveyed entirely within the channel, both during flood and ebb tides. In contrast, comparably

lower $|\vec{v}|$ values are found for water levels exceeding the bankfull depth $Y_B$, although relatively large $|\vec{v}|$ values occur when the high-tide water depth ($Y_H$) exceeds a critical value of about 3.2 m, that is, for tidal oscillations akin to spring-tide conditions (Figure 5a). When this happens, the vertical velocity profiles display significant variations, with reduced (enhanced) velocities found at water depths lower (higher) than $Y_B$.

The computed values of tidal flow asymmetries ($\rho_v$ and $\rho_d$) can be plotted as a function of the high-tide water depth ($Y_H$) observed during each monitored tidal cycle (Figure 5e,f,g). Made exception for the first monitored tidal cycle, flow velocities are found to be consistently flood-dominated for below-bankfull depths ($Y<Y_B$, Figure 5e). In contrast, ebb dominance becomes more common considering water depths above the bankfull ($Y>Y_B$), even though most of the data still falls within the flood-dominated domain (Figure 5f). Changes in high-tide water depth ($Y_H$) seem to not significantly affect peak flow asymmetry, although both data scattering and flood dominance appear to decrease slightly as $Y_H$ increases, both for above- and below-bankfull water depths (Figure 5e,f). Conversely, variations in $Y_H$ significantly affect tide duration asymmetry ($\rho_d$). The collected data suggest the persistence of flood-dominated conditions in our study channel during the entire monitoring period, with $\rho_d$ increasing proportionally to $Y_H$ in a statistically significant fashion (Figure 5g).

Stage-velocity diagrams for all the measuring stations display pronounced variations in the observed depth-averaged velocity (*DAV*), with *DAV* maxima typically occurring immediately below the bankfull water depth both for flood and ebb tides (Figure 6a,b,c,d). Flood *DAVs* are observed to decrease significantly once water depths exceed the bankfull stage. On the contrary, ebb *DAVs* rapidly increase once water depths become lower than the bankfull water depth. Although the peak *DAVs* are typically higher during the flood phase, which is in agreement with our previous observations regarding flow asymmetries, ebb *DAVs* attain near-maximum values for comparably longer times at water stages lower than bankfull (Figure 6a,b,c,d).

Similar to the *DAV* patterns, the rate of water-level change ($\dot{Y} = dY/dt$) peaks around the bankfull stage during the flood, whereas ebb peaks of $\dot{Y}$ are observed for water stages well above the bankfull (Figure 6e,f,g,h). Notably though, $\dot{Y}$ attains a nearly-constant value during most of the ebb phase, whereas much more pronounced changes are observed during the flood. A statistically significant, positive linear correlation is found between $\dot{Y}$ and *DAV* for below-bankfull stages

during both the ebb and the flood (Figure 6i,j,k,l), although such correlation is more robust for ebb flows (Figure 6i,j,k,l). For overbank stages, significant correlations between $\dot{Y}$ and *DAV* can only be obtained for the flood phase, whereas ebb *DAVs* are not significantly correlated to $\dot{Y}$ (Figure 6m,n,o,p).

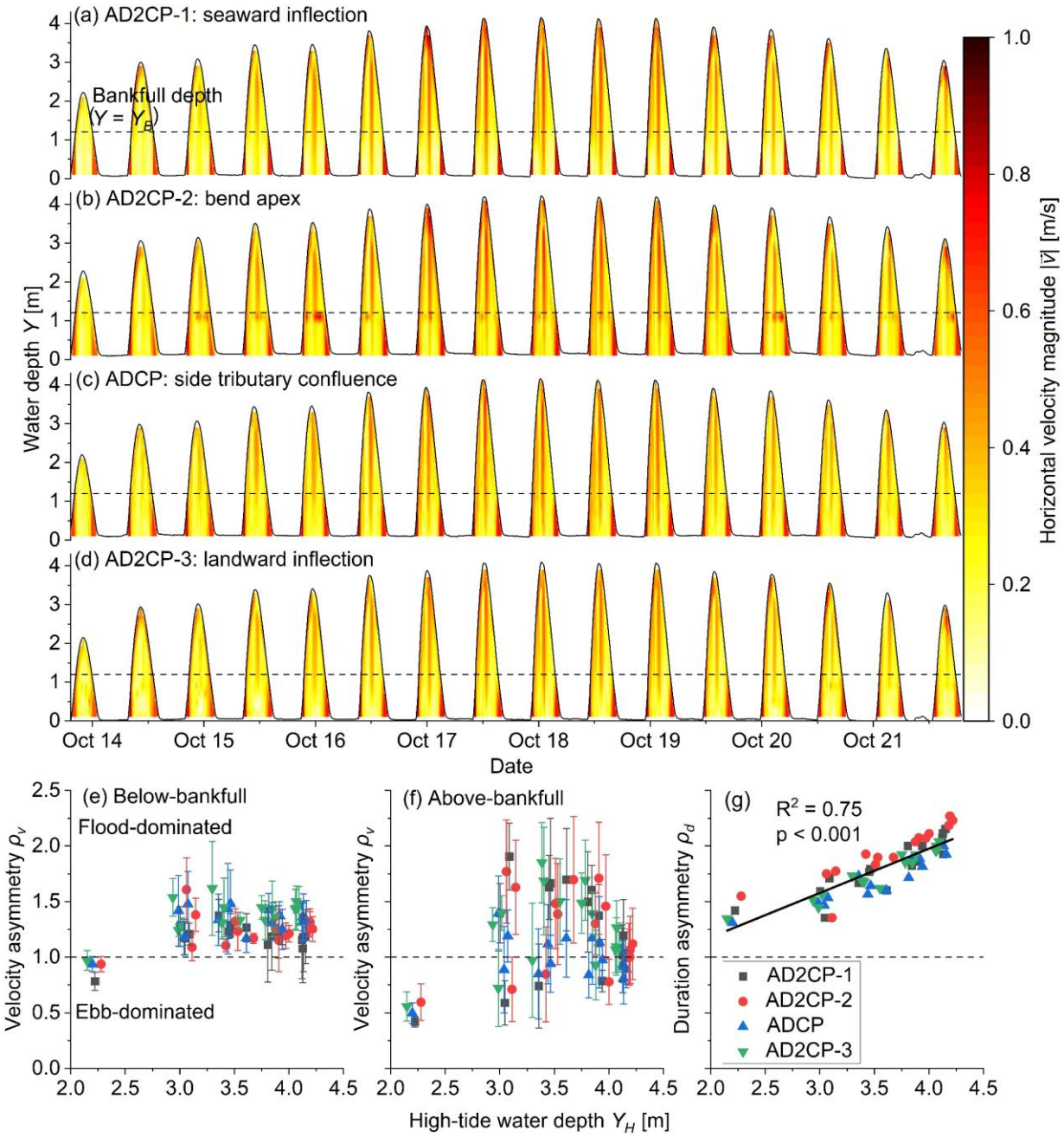

Figure 5. Time series of measured flow velocities and water depths. a,b,c,d) Time-continuous plots of horizontal velocity magnitudes ($|\vec{v}|$) as a function of instantaneous water depth ($Y$) for AD2CP-1 (seaward inflection point, panel a), AD2CP-2 (bend apex, panel b), ADCP (confluence with side tributary, panel c), and AD2CP-3 (landward inflection point, panel d). The horizontal velocity magnitude is computed as $|\vec{v}| = \sqrt[2]{|\overrightarrow{v_E}|^2 + |\overrightarrow{v_N}|^2}$, where $\overrightarrow{v_E}$ and $\overrightarrow{v_N}$ are the Eastward and Northward velocity components measured by the acoustic instruments, respectively. The horizontal, black-dashed line in each panel denotes water depth corresponding to the bankfull stage ($Y$=$Y_B$) for each measuring station. (e,f) Values of peak tidal velocity asymmetry ($\rho_v$) at different measuring stations are plotted against the high-tide water depth ($Y_H$) observed during each monitored tidal cycle. Panel e) shows $\rho_v$ for below-bankfull tidal flows, whereas $\rho_v$ values for above-bankfull flows are displayed in panel f). Data points represent the average value of $\rho_v$ computed at different depths, with error bars denoting standard deviation. (g) Values of tidal duration asymmetry ($\rho_d$) at different measuring stations are plotted against the high-tide water depth ($Y_H$) observed during each monitored tidal cycle. Different symbols and colors in panels e,f, and g denote different monitoring stations according to the legend in the lower-right inset. Calculations of tidal asymmetries were carried out only when instruments were submerged and both velocity and depth data could effectively be recorded.

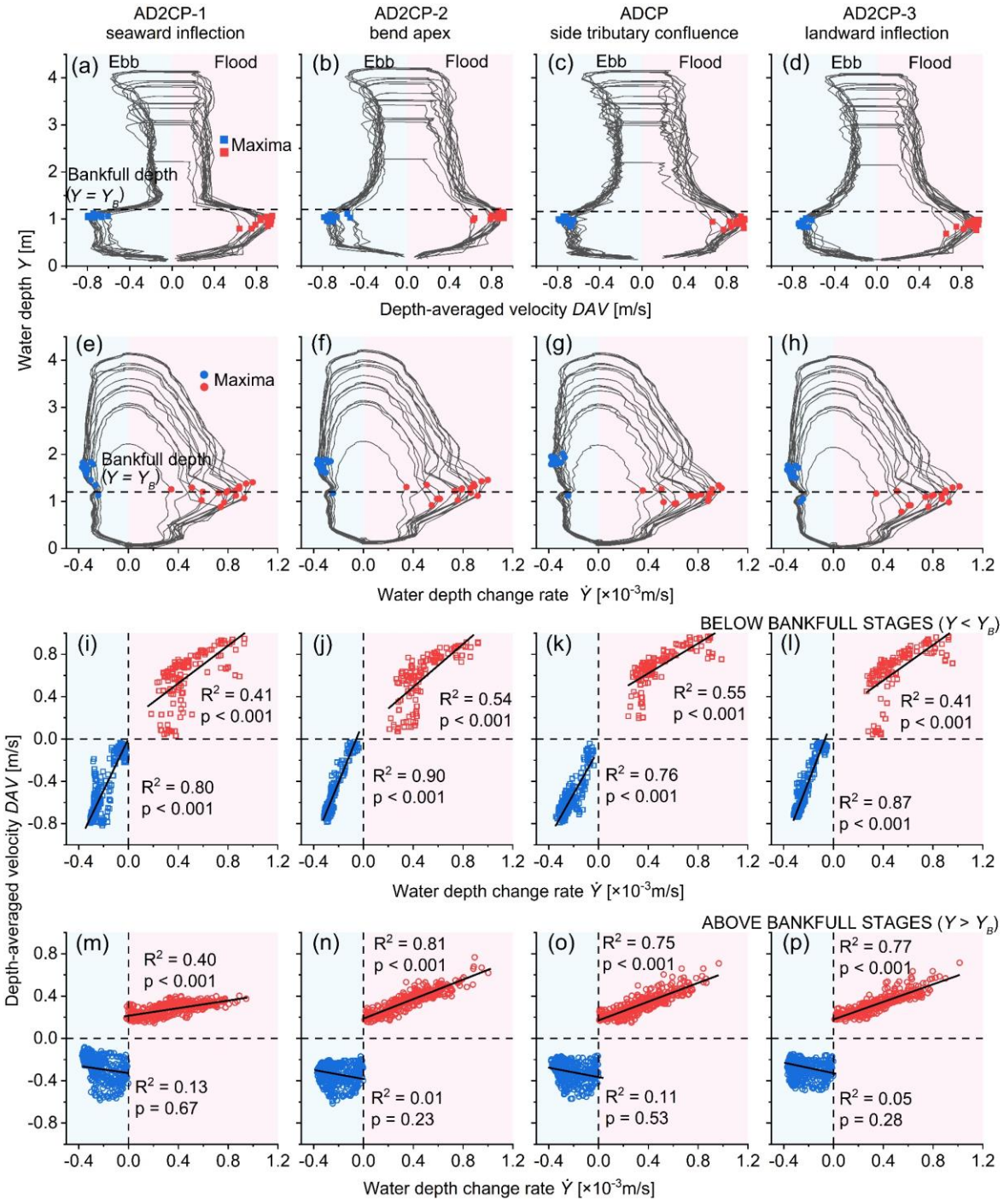


Figure 6. Relationships between depth-averaged velocity (*DAV*), water depth (*Y*), and water-depth change rate ($\dot{Y} = dY/dt$) at the four measuring stations. Columns from the left- to the right-hand side of the figure show, respectively, results for AD2CP-1 (seaward inflection point), AD2CP-2 (bend apex), ADCP (side tributary confluence), and AD2CP-3 (landward inflection point). Red and blue quadrants represent data obtained during the flood and the ebb phase, respectively. (a, b, c, d) Water depth (*Y*) vs. depth-averaged velocity (*DAV*) curves for all the monitored tidal cycles. Red and blue points denote the maximum flood and ebb *DAVs* of each tidal cycle. (e, f, g, h) Water depth (*Y*)

vs. water-depth change rate ($\dot{Y}$) curves for all the monitored tidal cycles. Red and blue points denote the maximum flood and ebb $\dot{Y}$ of each tidal cycle. (i, j, k, l) Depth-averaged velocity (*DAV*) as a function of water-depth change rate ($\dot{Y}$) for below-bankfull stages during all the monitored tidal cycles. (m, n, o, p) Depth-averaged velocity (*DAV*) as a function of water-depth change rate ($\dot{Y}$) for above-bankfull stages during all the monitored tidal cycles.

## 4.2 Phase averaged velocities and secondary circulations

### *4.2.1 Horizontal flow velocities*

Horizontal flow vectors $\vec{v}$ at different depths are plotted for high-amplitude (*HAT*) and low-amplitude (*LAT*) cycles separately (Figure 7c~f). At each measuring station, ebb and flood $\vec{v}$ for below-bankfull stages are generally characterized by similar orientations, yet with opposite directions, whereas more scattering is observed when flow depth exceeds the overbank stage. Directions of overbank flows appear to be consistent across different measuring stations, with flood and ebb flows directed to the southwest and southeast, respectively. In contrast, inter-site variability of below-bankfull flows is more marked, as $\vec{v}$ appears to follow the orientation of the channel axis, with $\vec{v}$ being more variable and generally less correlated to the channel axis orientation for near-bankfull conditions (i.e., water depths $0.8<Y<1.2$m). It is also worthwhile noting that flow directions at any given measuring station display little differences between *HAT* and *LAT* cycles, both for water stages above and below the bankfull.

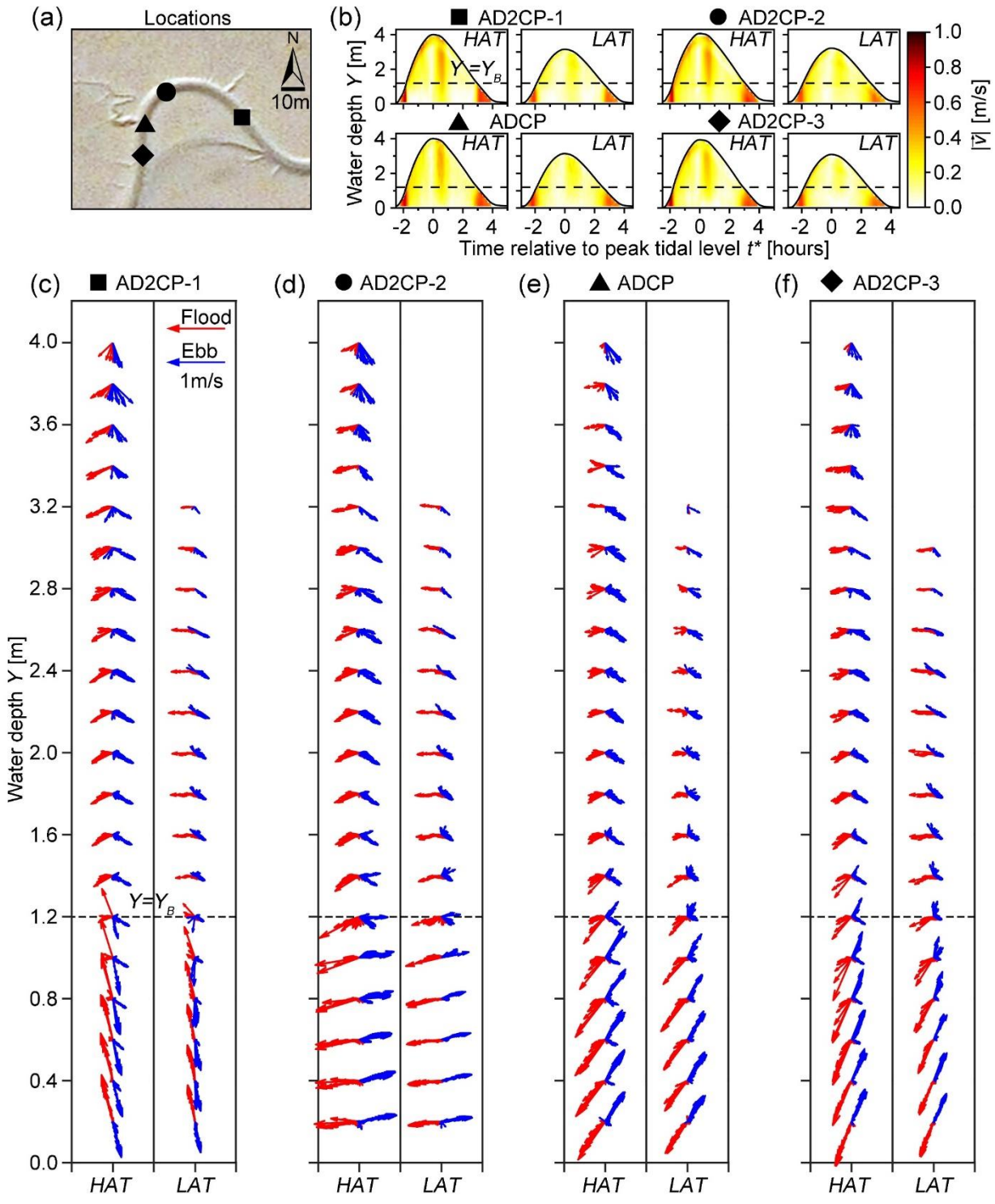


Figure 7. Ensemble phase-averaged horizontal velocity ($\vec{v}$) data at the four measuring stations. (a) Locations of measuring stations. (b) Time series of $\vec{v}$ magnitudes computed separately for high-amplitude tides (*HAT*) and low-amplitude tides (*LAT*) at each measuring station. (c,d,e,f). Vectors of horizontal velocities in *HAT* and *LAT* cycles plotted for different water depths ($Y$) at each measuring station during the ebb (blue) and flood (red).

438 *4.2.2 Streamwise velocities and secondary circulations*

439 In all the measuring sites, the primary (i.e., streamwise) velocity ($V_P$) reduces significantly once
440 the water stage reaches bankfull, both for *HAT* and *LAT* cycle. On the contrary, $V_S$ increases
441 significantly once water depth exceeds the bankfull (see panel b in Figures 8,9,10, and 11). To
442 better describe flow dynamics near the bankfull stage, we also plot $V_S$ vectors overimposed to $V_P$
443 magnitude values computed 15 minutes before and after the bankfull stage for both *HAT* and *LAT*
444 cycle (see panel c~f in Figures 8,9,10, and 11).

445 Velocity patterns observed at the seaward inflection site (AD2CP-1) are reported in Figure 8c~f.
446 During the flood, once the water depth exceeds the bankfull, $V_P$ decreases suddenly and even
447 reverses its direction in the upper layers, where $V_S$ increases significantly and takes direction
448 pointing toward the meander inner bank. In contrast, during the ebb, $V_S$ is very weak both for the
449 above- and below-bankfull stages (Figure 8c~f).
450 Similar results are observed at the landward inflection site (Figure 9). Particularly, peaks in $V_P$ are
451 observed for $Y<Y_B$, whereas the largest values of $V_S$ are attained when water depths exceed the
452 bankfull ($Y>Y_B$). During the flood, secondary velocities ($V_S$) are generally higher than at the
453 seaward inflection and consistently point to the outer bank in the upper vertical layers. Possible
454 secondary circulations emerge during the flood for both *HAT* and *LAT* cycles, with $V_S$ directed
455 toward the outer bank at the water surface and near the inner bank at the channel bottom. Overall,
456 data from both the landward and seaward inflection sites suggest the presence of secondary
457 circulations for overbank stages both for *HAT* and *LAT* cycles, with less obvious patterns being
458 observed during below-bankfull stages (Figure 8,9; see also Supplementary Figure S1a,b).
459 Secondary circulations can be observed at the bend apex (Figure 10), though they appear to be
460 generally weaker than those found at the bend inflections. During the flood, both $V_S$ magnitude
461 and secondary circulations are very weak when $Y<Y_B$ (Figure 10b~f and Figure S1c). Once
462 $Y$ reaches $Y_B$, $V_S$ increases and secondary circulations develop, especially during *HAT* cycles.
463 However, contrary to classic (i.e., fluvial) secondary circulation patterns where flows are directed
464 toward the outer bank in the uppermost portions of the water column, we observe secondary
465 circulations characterized by $V_S$ directed toward the inner bank near the water surface. During ebb
466 tides, $V_S$ are generally lower than during the flood, and secondary circulations are less clearly
467 noticeable both for *HAT* and *LAT* cycles.

468 Finally, at the confluence site, no significant secondary circulation is detected during either the
469 flood or the ebb, both for *HAT* and *LAT* cycles. During the flood, $V_S$ are consistently directed
470 toward the outer bank where the tributary is located and increase significantly when the water rises
471 above the bankfull stage (Figure 11b~f; see also Supplementary Figure S1d). In contrast, during
472 the ebb, a chaotic distribution of $V_S$ is found, with no clear indication of relevant secondary
473 circulations (Figure 11d,f, Figure S1d).

474

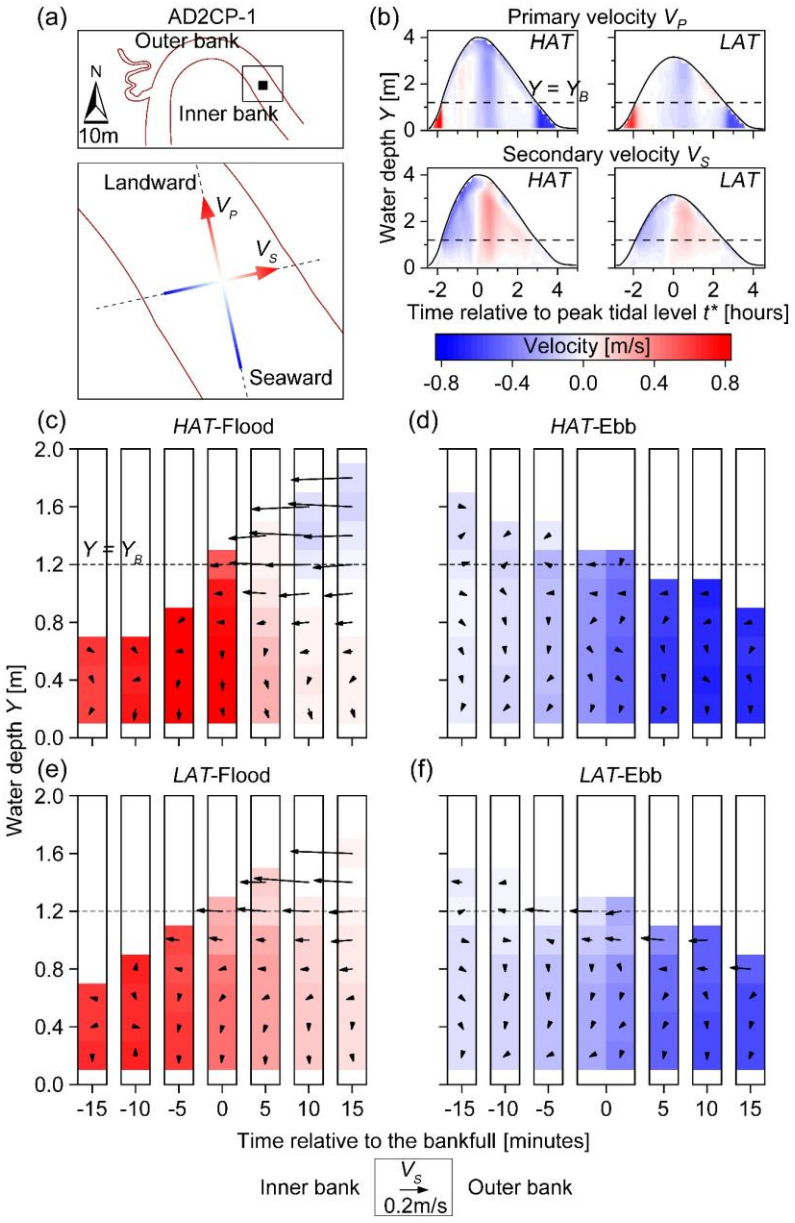


475

Figure 8. Flow decomposition at the seaward inflection site. (a) Location of AD2CP-1 and the direction of primary ($V_P$) and secondary velocity ($V_S$). (b) Time series of $V_P$ and $V_S$ during high-amplitude tide (*HAT*) and Low-amplitude tide (*LAT*). (c,d,e,f) Vertical distribution of $V_P$ magnitude with overimposed $V_S$ vectors computed, at 5-minute intervals, 15 minutes before and after the bankfull stage in the *HAT* and *LAT* cycle. $V_s$ are directed toward the inner and outer bank when pointing to the left- and right-hand sides of the figure, respectively.

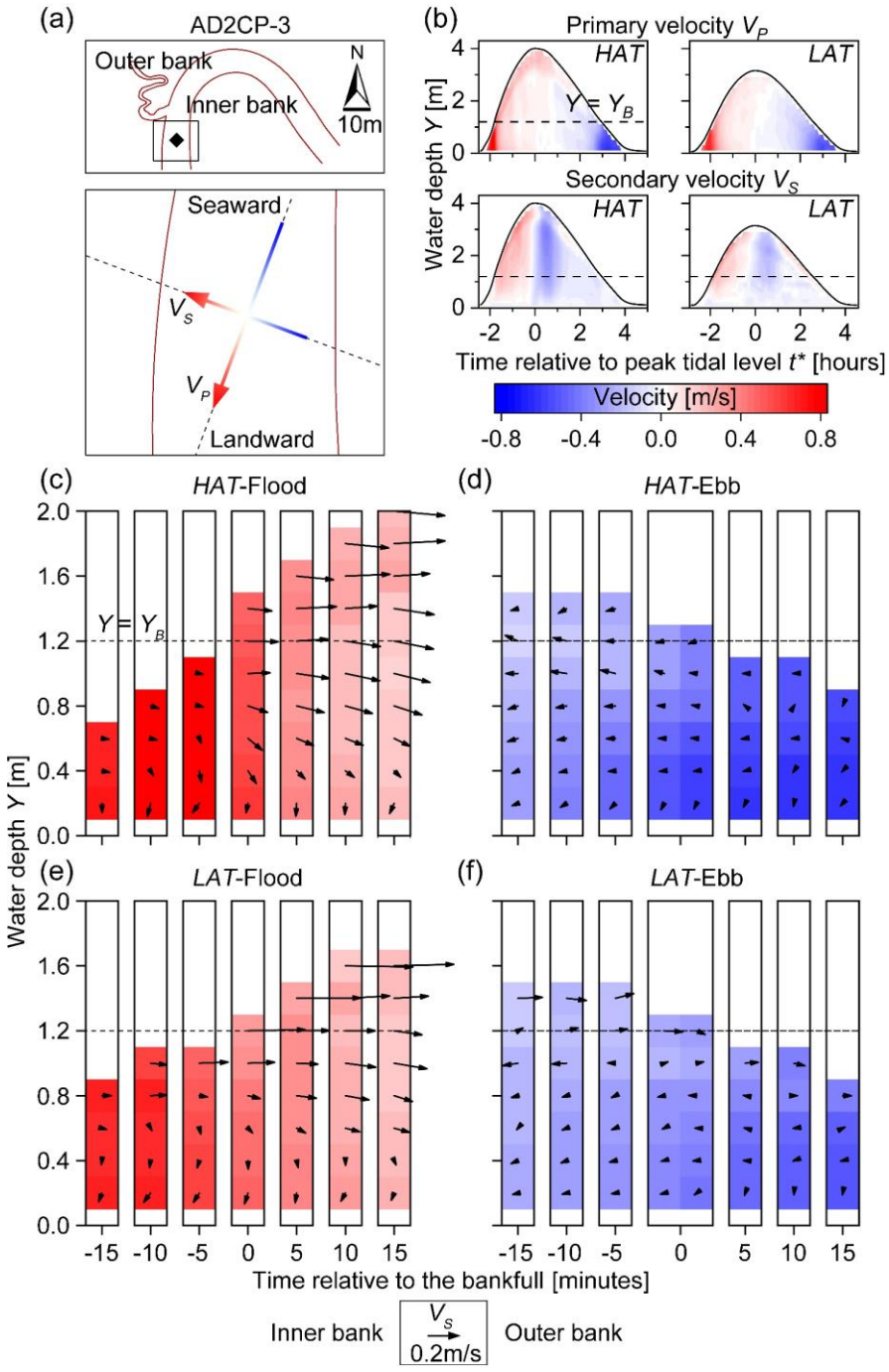

Figure 9. Flow decomposition at the landward inflection site. (a) Location of AD2CP-3 and the direction of primary ($V_P$) and secondary velocity ($V_S$). (b) Time series of $V_P$ and $V_S$ during high-amplitude tide (*HAT*) and Low-amplitude tide (*LAT*). (c,d,e,f) Vertical distribution of $V_P$ magnitude with overimposed $V_S$ vectors computed, at 5-minute intervals, 15 minutes before and after the bankfull stage in the *HAT* and *LAT* cycle. $V_s$ are directed toward the inner and outer bank when pointing to the left- and right-hand sides of the figure, respectively.

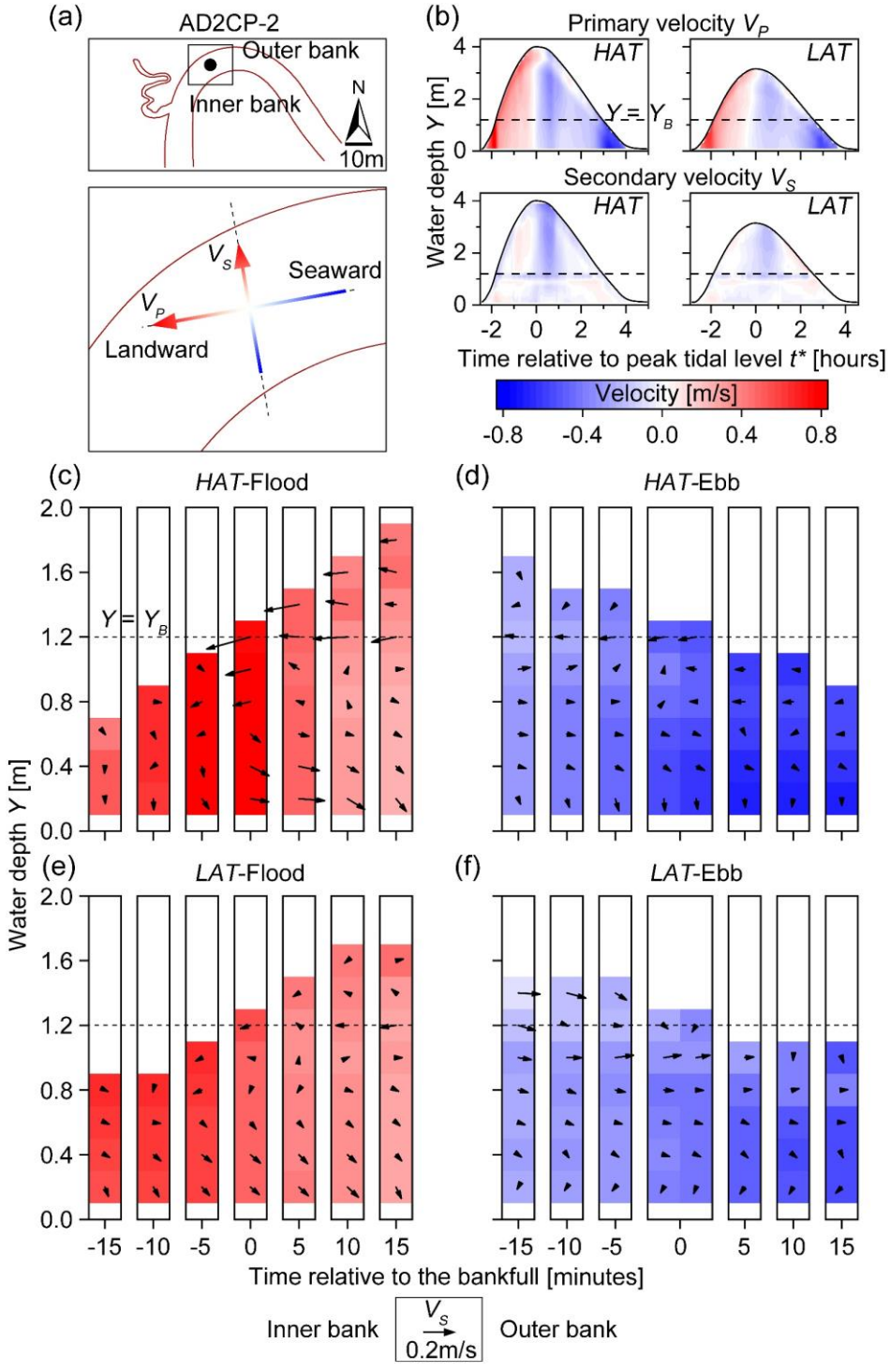

Figure 10. Flow decomposition at the apex site. (a) Location of AD2CP-2 and the direction of primary ($V_P$) and secondary velocity ($V_S$). (b) Time series of $V_P$ and $V_S$ during high-amplitude tide (*HAT*) and Low-amplitude tide (*LAT*). (c,d,e,f) Vertical distribution of $V_P$ magnitude with overimposed $V_S$ vectors computed, at 5-minute intervals, 15 minutes before and after the bankfull stage in the *HAT* and *LAT* cycle. $V_s$ are directed toward the inner and outer bank when pointing to the left- and right-hand sides of the figure, respectively.

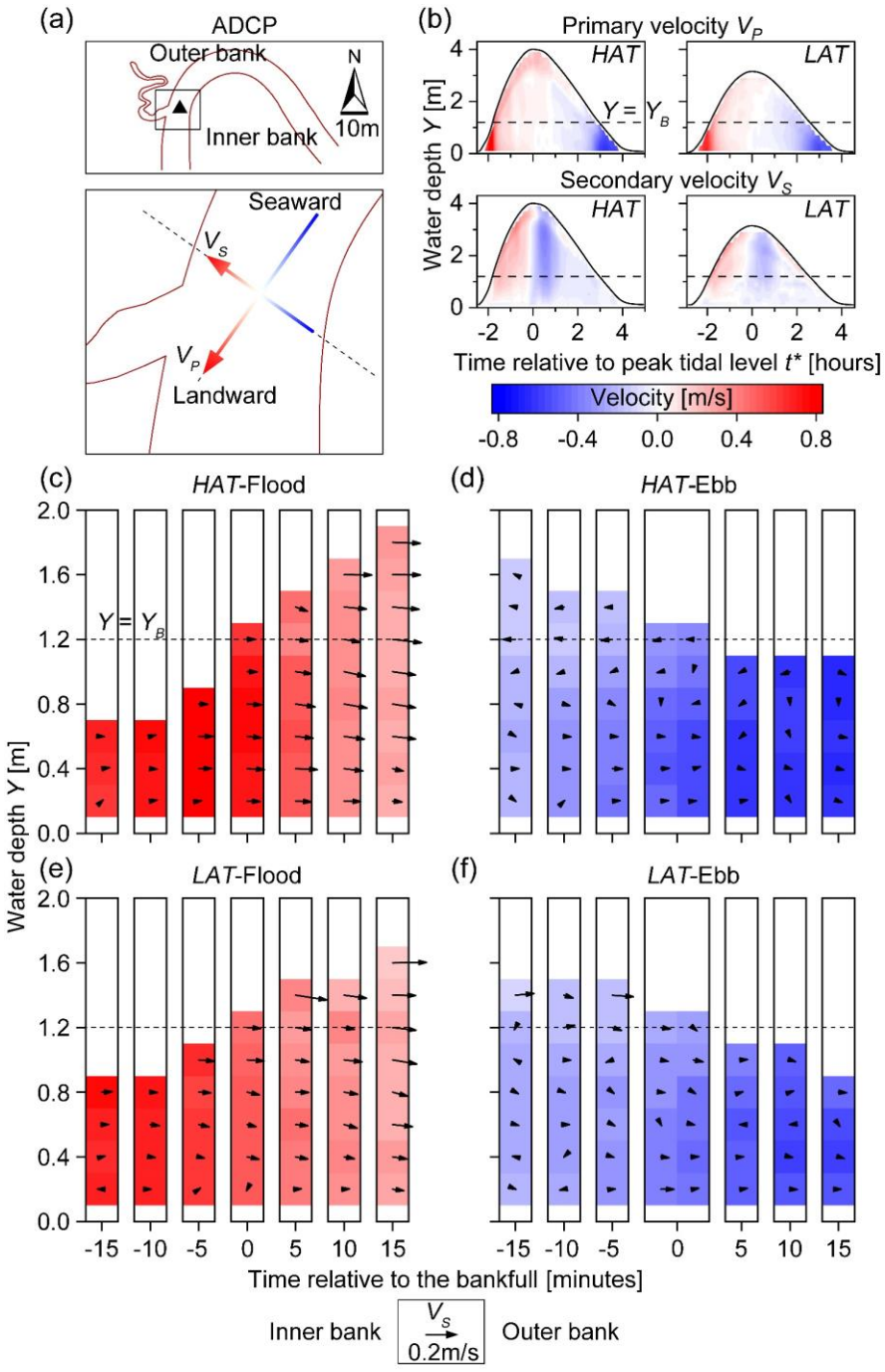

Figure 11. Flow decomposition at the confluence site. (a) Location of ADCP and the direction of primary ($V_P$) and secondary velocity ($V_S$). (b) Time series of $V_P$ and $V_S$ during high-amplitude tide (*HAT*) and Low-amplitude tide (*LAT*). (c,d,e,f) Vertical distribution of $V_P$ magnitude with overimposed $V_S$ vectors computed, at 5-minute intervals, 15 minutes before and after the bankfull stage in the *HAT* and *LAT* cycle. $V_s$ are directed toward the inner and outer bank when pointing to the left- and right-hand sides of the figure, respectively.

## 5 Discussions

### 5.1 Overbank flows and stage-velocity relationships

Horizontal velocity distributions and stage-velocity diagrams of our studied channel display critical differences compared to those observed in channels wandering through vegetated salt marshes and mangrove forests (D'Alpaos et al., 2021; Fagherazzi et al., 2008; Hughes, 2012; Kearney et al., 2017; McLachlan et al., 2020; van Maanen et al., 2015; see Figures 5 and 6). Owing to the characteristic geomorphic structure of vegetated intertidal plains, peaks of ebb and flood velocities in tidal channels typically occur just below or above the bankfull stage (i.e., for $Y>Y_B$), with velocities being significantly reduced at $Y<Y_B$ and approaching null values when $Y$ is minimum (see Bayliss-Smith et al., 1979; Boon, 1975; Fagherazzi et al., 2008; Hughes, 2012; Kearney et al., 2017). In contrast, our monitored mudflat channel is characterized by sustained velocities at $Y<Y_B$, with both horizontal ($\vec{v}$) and depth-averaged velocities ($DAVs$) peaks occurring when tidal flows are confined within the channel banks (Figures 5 and 6). Notably, in all the monitored sites velocities are relevant ($DAV\approx0.8$ m/s) even for reduced water depth ($Y<0.5$ m), especially during the ebb (see Figure 6a,b,c,d). Overbank stages are instead characterized by reduced velocities, both in terms of $\vec{v}$ and $DAV$ values (Figures 5 and 6).

These discrepancies in velocities fields between channels found in vegetated and unvegetated intertidal settings are likely due to the relative speed at which tides can propagate within and outside tidal channel networks. Specifically, frictionally-dominated tidal flows across vegetated intertidal plains make channels preferential pathways for tide propagation even when water levels exceed the bankfull (i.e., for $Y>Y_B$; D'Alpaos et al., 2007; Rinaldo et al., 1999a, 1999b). In contrast, flow resistance in unvegetated mudflats is comparable between tidal channels and intertidal plains, such that tide propagation through unvegetated intertidal mudflats is dominated by sheet flow. This hypothesis is supported by field data from the meso-macrotidal Scheldt Estuary

(Vandenbruwaene et al., 2015) highlighting similar velocities within tidal channels (0.3~1 m/s) and across bare intertidal mudflats (0.1~0.4 m/s), in contrast to salt marshes wherein tidal flow velocities are typically lower than 0.1 m/s. In our studied channel, flow velocities for above- and below-bankfull stages are found to be in the range 0.2~0.4 m/s and 0.2~1 m/s, respectively (Figure 5,6), which roughly correspond with the results of Vandenbruwaene et al. (2015). The latter data also suggest that instantaneous water levels are not significantly different within channels and across mudflats, in contrast to frictionally-dominated vegetated intertidal plains where significant differences in instantaneous water levels occur moving away from tidal channels (D'Alpaos et al., 2021; Rinaldo et al., 1999a, 1999b; Sullivan et al., 2015).

Besides differences in bottom friction at overbank stages, one should also appreciate that hydrodynamic dissimilarities are to be expected in mudflat vs. salt-marsh channels as a consequence of distinct characteristic elevations of both their banks and the adjoining intertidal platforms. Mudflat channels typically occupy the lower portions of the intertidal frame, their bank elevation typically ranging between the mean sea level (MSL) and the mean low water springs (MLWS). This allows for significant water depths at above-bankfull stages, which reduce flow confinement within the channel and limit channel flow velocities (Brooks et al., 2021). In contrast, channel banks in salt marshes are typically located in the highest portions of the intertidal frame, which ensures in-channel flow confinement and sustained flow velocities even for large tidal oscillations, effectively limiting above-bankfull water depths. In our study case, high $\vec{v}$ during overbank stages are only observed when peak tidal levels exceed $Y_{max}$>3.2 m, that is, for spring tidal cycles (Figure 4a,b,c,d) or, more generally, for high-amplitude (*HAT*) tidal cycles (Figure 7b). Such high $\vec{v}$ values are however likely related to overbank circulations occurring at the scale of the entire mudflat systems, which are not necessarily related to flow dynamics within the channel. This is confirmed by the analysis of $\vec{v}$ directions along the water column (Figure 7c), which testifies clear deviations of tidal flows at $Y>Y_B$ relative to the orientation of the channel axis both for *HAT* and *LAT* tidal cycles. Such a deviation produces consistent flow directions in all the monitored sites, with tidal flows being directed to the South-East and South-West during ebb and flood tides, respectively (Figure 7c).

These observations altogether support the idea that differences in the character of overbank flows result in marked hydrodynamic dissimilarities between tidal channels dissecting vegetated and

unvegetated intertidal plains. Such differences are also likely to affect curvature-induced secondary circulations and the related meander morphodynamic evolution, as we discuss in detail in the next sections.

### 5.2 Secondary circulations and curvature-induced helical flows

According to classic flow fields observed in sinuous channels, secondary (i.e., cross-sectional) circulations are observed in our study bend, both during high-amplitude (*HAT)* and low-amplitude (*LAT*) tidal cycles (Figures 8,9,10,11). These secondary circulations are more pronounced during overbank stages, their intensity increasing as the water depth increases within the studied channel. Indeed, secondary circulations tend to be stronger for *HAT* than *LAT* cycles (Figures 8,9,10,11). They also appear to be mostly related to flood flows, which is in agreement with the generally flood-dominated character of tidal flows observed in the studied bend (Figure 5e,f,g). In some cases, the orientation of secondary circulations is reversed compared to classic flow models such as, for example, at the seaward bend inflection as well as at the meander apex (Figure 8 and Figure 10), where secondary circulations are directed toward the inner and outer bank at the top and bottom of the water column, respectively. Secondary currents can trigger cross-sectional sediment transport processes such that fine-grained deposits are transported up to the point bar from the channel bed, giving rise to fining upward trends due to the progressive upbar weakening of secondary currents (Bathurst et al., 1977; Blanckaert, 2011; Dietrich, 1987; Termini & Piraino, 2011). This is supported by the fining upward trends that are consistently observed from sediment cores collected at different sites along the studied bend (Figure 3).

Interestingly, secondary circulations are more pronounced at the meander inflections than at the apex, where they should be stronger owing to higher channel curvature. This could however depend on the surveying strategy we used, since we only monitored the velocity profile in correspondence to the channel axis rather than across the entire cross-section. Previous studies have demonstrated that secondary circulation cells do not necessarily occupy the whole channel cross-section (e.g., Blanckaert, 2009, 2011; Finotello, Ghinassi, et al., 2020). Particularly, hydrodynamic nonlinearities can arise in sharp bends characterized by radius-to-width ratios $R/\overline{W}$ lower than 2-3, and flow separation may occur either at the inner or outer bank, respectively,

immediately upstream or downstream of the bend apex (Blanckaert et al., 2013; Finotello, Ghinassi, et al., 2020; Hickin, 1978; Hickin & Nanson, 1975; Hooke, 2013; Parsons et al., 2004; Rozovskiĭ, 1957). Flow separation, which is common in tidal meanders owing to the high curvature values that they typically display (Ferguson et al., 2003; Finotello, D'Alpaos, et al., 2019), can effectively reduce the portion of the channel that is hydrodynamically active and confine curvature-induced secondary circulations to the nonrecirculating portion of the primary flow (Finotello, Ghinassi, et al., 2020; Leeder & Bridges, 1975; Parsons et al., 2004). Our studied meander bend is characterized by a $R/\overline{W}$=2.2, and the formation of flow sepeartion is therefore highly likely. Direct measurement of tidal flows across the entire channel cross section would be necessary to settle the dispute, but such data are hard to collect because channel banks at our studied site are flooded by more than 3 m of water at high tides, thus making field measuring campaigns complicated. Nevertheless, we can still estimate the chance for flow separation at the apex of our studied channel by comparing our data with the results obtained by Leeder and Bridges (1975) for intertidal meanders in the vegetated Solway Firth (Scotland). According to Leeder and Bridges (1975), the chances for flow separation in tidal meander bends can be expressed as a function of bend tightness ($R/W$) and Froude number ($Fr$). Although extending the results of Leeder and Bridges (1975) to unvegetated mudflats might not be entirely appropriate, results would still offer useful insights on the possible occurrence of flow separation, especially for below-bankfull stages when tidal flows are confined within the channel. Since our measurements include several consecutive tidal cycles, we were able to calculate how the $R/W$ changes according to varying water depths. Specifically, we assumed that $R$ does not vary significantly with changing water elevation, and we computed the channel width $W_Y$ corresponding to different water depths ($Y$) based on topographic data of the meander-apex cross-section (Figure 4b). Plotting of $R/W_Y$ against $Fr$ shows that flow separations at the bend apex site are likely to occur at near-bankfull stages (Figure 12). This is clearly related to the morphology of the studied bend, which is characterized by a relatively low width-to-depth ratio ($\beta$), whereby $W_Y$ increases rapidly as $Y$ increases, thus producing progressively lower $R/W_Y$ in the range from 8 to 2. In addition, flow velocities at the below-bankfull stage generate a modest $Fr$ value of 0.2~0.3, which can possibly induce flow separations (Leeder & Bridges, 1975). In contrast to our observations, Figure 12 suggests that flow separation will be suppressed at overbank stages, likely because of the observed flow velocity reduction at $Y>Y_B$. Care should be however given when extending the results proposed by Leeder and Bridges (1975) to situations where tidal

flows do not remain confined within channel banks. Regardless, our analyses support the idea that reduce secondary circulations observed at the meander apex could be ascribed to flow separation, which makes secondary circulations hard to identify through localized flow measurements.

Regardless of flow separation, it is worthwhile noting that secondary circulations are stronger during overbank stages, when flow confinement within channel banks is significantly reduced and, as a result, primary velocities ($V_P$) are small. Thus, there seems to be a phase shift between peaks of primary ($V_P$) and secondary velocity ($V_S$), such that $V_P$ is maximum when $V_S$ is low, and vice versa. Such a shift would effectively limit the advection of cross-stream circulations operated by the primary flow, thus hampering the formation of characteristic curvature-induced helical flows (e.g., Blanckaert, 2011; Blanckaert & de Vriend, 2003; Dinehart & Burau, 2005; Ferguson et al., 2003; Frothingham & Rhoads, 2003). Moreover, we notice that primary velocities at overbank stages are sometimes characterized by reverse direction relative to below-bankfull stages, that is, $V_P$ are directed seaward (landward) during flood (ebb) tides (see for example Figure 8c). This would further limit the transfer of secondary circulation by primary velocity along the meander bend, thus hampering the formation of helical flows even further. Such behavior has not been observed in tidal channels flanked by vegetated intertidal plain, wherein $V_P$ and $V_S$ maxima are approximately in phase and correspond roughly to near-bankfull water stages (e.g., Fagherazzi et al., 2008; Finotello, Ghinassi, et al., 2020; Kearney et al., 2017). Additionally, secondary circulations also appear poorly developed at the confluence site. It is well known that complex circulation patterns can arise at channel confluences (e.g., Lane et al., 2000; Leite Ribeiro et al., 2012; Rhoads & Kenworthy, 1995; Schindfessel et al., 2015), which are likely to suppress curvature-induced secondary flows. Nonetheless, one should appreciate that channel confluences in intertidal mudflat channel networks are somehow less frequent than in networks carving vegetated intertidal plains, owing to the lower drainage density that characterizes bare intertidal areas (e.g., Kearney & Fagherazzi, 2016). Therefore, flow disturbances and helical flow disruption due to channel confluences and bifurcations are not likely to have a significant limiting effect on meander morphodynamics in intertidal mudflats.

Overall, the results we illustrated so far suggest poor development of curvature-induced secondary flows in intertidal mudflat meander bends. The implications of this hydrodynamic peculiarity, as well as those highlighted in Section 5.1, for the morphodynamics of intertidal mudflat meanders, will be discussed in the next section.

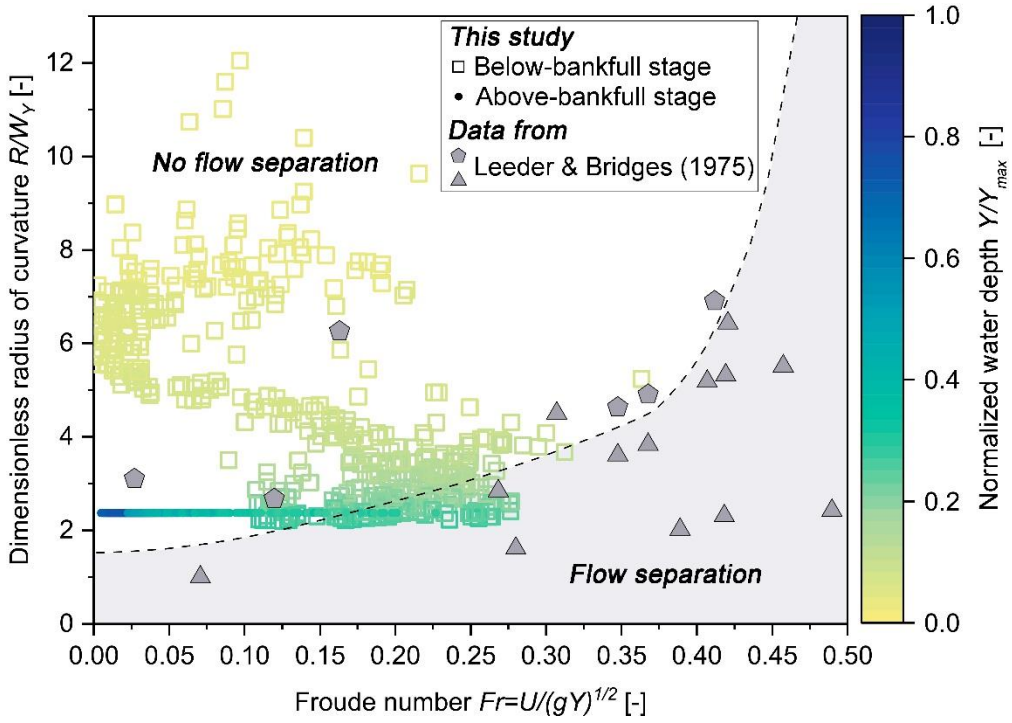


Figure 12. Flow separation in tidal meander bends according to Leeder & Bridges (1975). The normalized radius of curvature ($R/W_Y$) is plotted as a function of Froude number ($Fr$) for distinct tidal flow depth ($Y$) and velocity ($U$) at the apex of the studied meander bend. The parameter $W_Y$ represents the effective bend width corresponding to different water depths ($Y$), whereas $Fr$ is calculated for different water depths $Y$ and the corresponding uniform flow velocities $U$, the latter being approximated by the depth-averaged velocity ($DAV$). Colors denote varying normalized water depths, computed as the ratio between instantaneous water depths and the maximum water depth ($Y_{max}$) observed during the entire monitoring timespan. Filled dots denote below-bankfull water stages ($Y<Y_B$, where $Y_B$ is the bankfull depth), whereas empty squares highlight above-bankfull stages ($Y>Y_B$). Original data points from Leeder and Bridges (1975) are also reported using gray markers, along with their empirical line separating bends with and without flow separation.

### 5.3 Implications for meander morphodynamics

Since the generation and propagation of helical flow are hampered, questions arise regarding what are the chief morphodynamic processes driving meander evolution in unvegetated intertidal mudflats. Previous studies suggested that mudflat meanders can form and develop without significant secondary circulations. For example, the evolution of small mudflat meandering channels (about 1 m wide) in the Westerschelde estuary (Netherlands) was found to be primarily

driven by late-ebb flows, which determined the erosion of channel bed due to backward-migrating steps generated by hydraulic jumps, which in turn promoted channel bank erosion due to bank undercutting and pronounced flow separation in sharp bends (Kleinhans et al., 2009). In our studied channel, sustained velocities at low water stages (Figures 5,6,8,9,10,11), together with direct visual inspections of sustained flow velocities near the end of ebb tides (see Figure 4), support the idea proposed by Kleinhans et al. (2009) that the morphodynamics of intertidal mudflat meanders is strongly controlled by late-ebb flows rather than by classic bar-hugging helical flow produced by curvature-induced secondary flows at high-water stages. Reduced control of helical flows on channel morphodynamics is also testified by the symmetric, V-shaped form of the studied channel cross-sections (Figure 4b), which attests to the scarce development of secondary (i.e., cross-sectional) flows and contrasts with the asymmetrical U-shaped cross-sections displayed by meandering channels in vegetated tidal marshes (Finotello, Ghinassi, et al., 2020; Zhao et al., 2022).

In contrast to late-ebb flows, we speculate that tidal flows at early-flood stages are not likely to have significant effects in terms of bank undercutting and sediment transport because velocities increase more slowly than during late ebb, and rates of water depth change through time ($\dot{Y}$), though sustained, do not produce significant variations in $DAVs$ (Figure 6). Our analyses indeed confirm that tidal flows tend to be ebb-dominated at low water depths (Figure 5e,f), and also highlight that at $Y<Y_B$ ebb velocities attain values close to the maximum for much longer periods than during the flood (Figure 6), thus likely enhancing the morphodynamic control of late-ebb flows on channel evolution. Moreover, late-ebb flows are likely to occur even for tidal oscillations lower than those we monitored here, whereas pronounced overbank flows and related secondary circulations require significant tidal oscillations to be formed. Because intense late-ebb flows act at every tidal cycle and operate for extended periods, the total morphodynamic work they produce is in all likelihood much more significant than that produced during other tidal phases, further supporting the hypothesis that late-ebb tidal stages are the most morphodynamically relevant for mudflat meander evolution.

The above-described morphodynamic control of late-ebb stages is likely to be even more relevant compared to vegetated tidal landscapes due to the absence of vegetation not only on intertidal plains but also within tidal channels. In fact, previous studies focusing on salt-marsh channels

696 demonstrated how in-channel aquatic vegetation can enhance bottom roughness and flow
697 turbulence (e.g., Finotello, Ghinassi, et al., 2020; Folkard, 2005), further limiting tidal flow
698 velocities at low stages, especially in relatively small channels with widths comparable to the
699 characteristic size of vegetation patches. The presence of aquatic vegetation would clearly prevent
700 significant morphodynamic work to be performed by late-ebb tidal stages, which is likely not the
701 case in the unvegetated mudflat channel we investigated here.

702 In addition to the above, meander morphodynamics in unvegetated intertidal flats can also be
703 driven by episodic and seasonal increases in discharges due to heavy rainfalls and melting snows
704 (Choi et al., 2013; Choi & Jo, 2015). Choi (2011, 2014) observed that these episodic events are
705 likely to cause abrupt morphologic changes, pronounced point bar migration, frequent meander-
706 bend cutoff, as well as channel abandonments. Particularly, significant rainfall-induced runoff
707 during low tides would mimick late-ebb flows, thus further increasing the morphodynamic
708 relevance of seaward-directed, shallow, in-channel flows. New field measurements will however
709 be required to support this hypothesis in the Yangkou tidal flat, since the data presented in this
710 study were collected in October, which is outside the monsoon season.

711 Storm waves could also induce bank collapses in unvegetated tidal channels (Choi, 2011; Choi &
712 Jo, 2015; Ghinassi et al., 2019), thus critically affecting meander morpho-sedimentary evolution.
713 In spite of the absence of vegetation that can help stabilize banks and prevent erosion, no collapsed
714 slump blocks were observed within our study channel (Gabet, 1998; Hackney et al., 2015),
715 although such blocks could be easily disgregated and removed, once formed, by sustained in-
716 channel velocities combined with the absence of additional cohesion given by vegetation roots.

717 Bank collapses can also form due to significant tidal oscillations and pore-excess pressure between
718 channel and banks driven by rapid changes in water levels (Zhao et al., 2022; Zhao et al., 2019),
719 which generate significant seepage flows (e.g., Gardner & Wilson, 2006; Wilson & Morris, 2012).
720 Seepage flows during late-ebb tides, also favored by extensive bioturbation due to fiddler-crab and
721 mudskipper burrowing (Harvey et al., 2019; Ishimatsu et al., 1998; Perillo et al., 2005; Xin et al.,
722 2022), are likely responsible for the widespread bank slumps that we observed at the middle and
723 lower portions of channel cross-sections in the studied channel (Figure 13). Notably, strong
724 seepage flows can also help explain why sustained velocities are observed over nearly the entire

duration of the ebb phase (Figure 6 a,b,c,d), and further support the idea that the ebb-late phases exert a strong control on the morphodynamics of intertidal mudflat meanders.

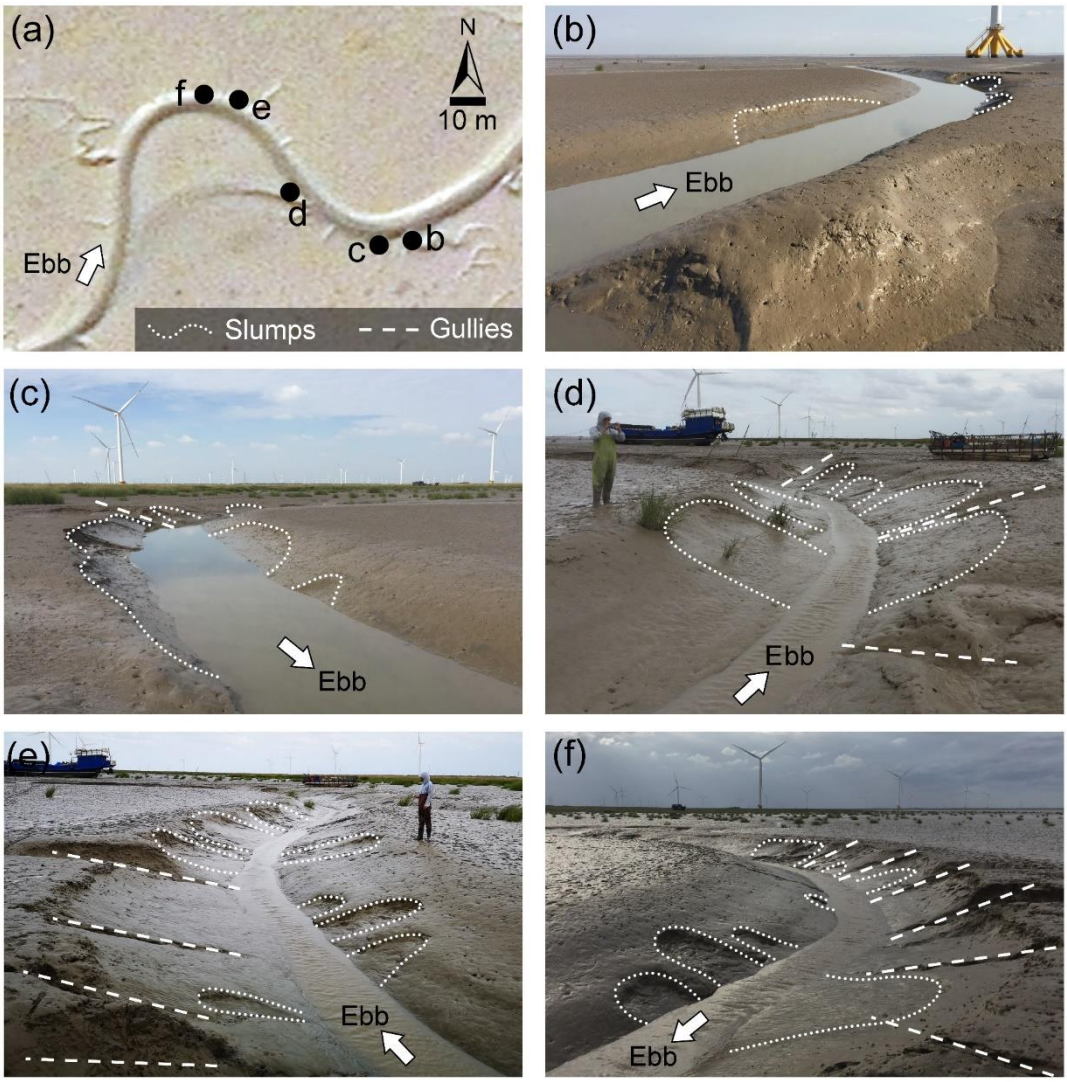


Figure 13. Bank erosion along the studied channel. (a) Locations of the photographs. (b,c,d,e,f) Close-up views of bank slumps (white dotted lines) and gullies (white dashed lines) along the studied channel. All photos were taken during ebb tides.

If, on the one hand, bank collapses driven by seepage flow are also commonly documented in vegetated macrotidal settings (Cosma et al., 2022; Zhao et al., 2022) and are therefore more closely linked to sustained tidal oscillations, on the other hand, the abundant erosional gullies (Figure 13) observed at channel banks are most likely specific of unvegetated settings. The formation of such

736 gullies, which can significantly contribute to bank erosion processes, is promoted by strong erosion
737 at the ebb-bankfull transition and favored by the absence of vegetation cover (Guimond &
738 Tamborski, 2021). Bank collapses and gullies can also be counterintuitively related to the presence
739 of cohesive extracellular polymeric substances (EPS) generated by microorganisms abundant on
740 intertidal flats. However, although EPS are widely regarded as bed "stabilizers" (Flemming &
741 Wuertz, 2019), recent flume experiments show that they may enhance sediment mobility under
742 wave actions, inducing liquefaction of otherwise stable bank sediment (Chen et al., 2021), with
743 clear implications for the dynamics of meandering tidal channels.

744 Overall, our results support the idea that meander evolution in intertidal mudflats might not be
745 necessarily correlated with classic curvature-induced helical flows at near-bankfull stages, and that
746 other ecomorphodynamic factors, most likely related to tidal hydrodynamics at late-ebb stages,
747 can be more relevant for meander morphodynamics. A synthesis of the main hydrodynamic
748 characteristics of meandering channels developed in vegetated and unvegetated intertidal plains,
749 and the differences thereof, is reported in Table 2. In addition, a conceptual summary sketch
750 illustrating the major hydrodynamic and morphodynamic differences between tidal meandering
751 channels in vegetated and unvegetated contexts is shown in Figure 14. Further analyses will be
752 needed to corroborate the inferences presented in this study, as well as to investigate the role played
753 by different tidal amplitudes on the processes we described here, especially in terms of distinct
754 hydrodynamic behavior between above and below-bankfull stages. Nonetheless, large tidal ranges
755 (relative to characteristic wind-wave heights) are needed for the development of intertidal mudflats
756 (e.g., Friedrichs, 2011; Klein, 1985; Morales, 2022), so we argue that the processes observed in
757 the present study are likely to be common also in intertidal mudflat channels different from the
758 study case we analyzed here.

759

760

761

762

763

764 Table 2. Comparison of the major hydrodynamic characteristics of meandering tidal channels
765 wandering through vegetated (e.g., salt marshes) and unvegetated (e.g., mudflat) intertidal plains

| | *Vegetated intertidal plains* | *Unvegetated intertidal plains* |
|---|---|---|
| Overbank flow | Low frequency of occurrence (only for the highest tides) | High frequency of occurrence (almost every tidal cycle) |
| | Relatively shallow water depth ($Y_{MAX}$<1 m) | Relatively large water depths ($Y_{MAX}$>3-4 m) |
| | Weak and frictionally-dominated flow ($v_{MAX}$ =0.1-0.2 m/s) | Strong and sheet-flow-dominated flow ($v_{MAX}$ >0.4-0.5m/s) |
| | Flow direction nearly perpendicular to the channel-axis orientation | Flow direction virtually unrelated to the channel-axis orientation |
| Stage-velocity relation | Higher velocities for above-bankfull stages ($Y$>$Y_B$) | Higher velocities for below-bankfull stages ($Y$<$Y_B$) |
| Secondary circulations | Relatively strong | Relatively weak |
| | More pronounced when primary streamwise flows are stronger (i.e., in phase with streamwise flows) | More pronounced when primary flows are weaker (i.e., out of phase with streamwise flows) |
| Helical flow | Well developed | Poorly developed |
| Flow separation | Possible as a function of bend geometry and tidal flow characteristics (i.e, Froude number) | Possible as a function of bend geometry and tidal flow characteristics (i.e, Froude number) |
| Rainfall runoff | Limited importance due to the presence of vegetation | Potentially significant due to the absence of vegetation |
| Wave action on intertidal plains | Weak due to wave attenuation by vegetation | Strong due to high overbank water depths and reduced friction |

766

767

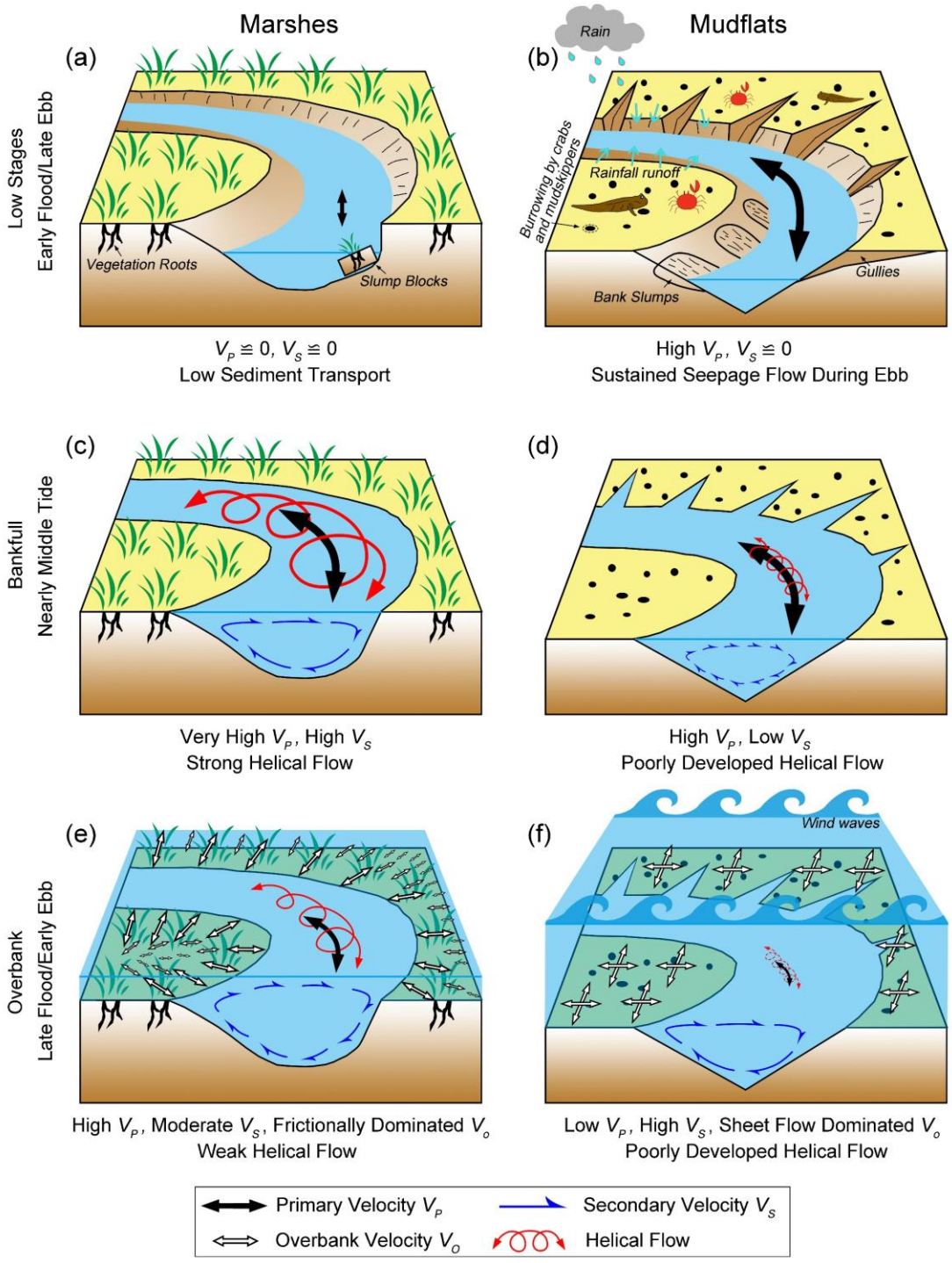


Figure 14. Conceptual sketch depicting the major differences of hydrodynamic processes observed in tidal channels dissecting vegetated (i.e., salt marshes, left columns) and unvegetated (i.e., mudflats, right columns) intertidal plains. (a, b) Channel hydrodynamics during below-bankfull water stages, with particular reference to early-flood and late-ebb stages; (c, d) Channel hydrodynamics at the bankfull stage; (e, f) Channel hydrodynamics during overbank stages.

## 6 Conclusions

This study contributes to the understanding of hydrodynamic flow structures, and related morphodynamic evolution, in meandering channels wandering through unvegetated tidal flats. Hydroacoustic measurements were carried out, for several tidal cycles, at distinct locations along a mudflat meander bend found within the macrotidal Yangkou tidal flat (Jiangsu province, China). The main conclusions of this research can be summarized as follows:

(1) Stage-velocity relationships in mudflat channels are different from those observed in channels wandering through vegetated intertidal plains (i.e., salt marsh and mangrove forests). Specifically, while in the latter case both ebb and flood velocities tend to be higher for above-bankfull water stages, in our study case we observed significantly larger velocities when tidal flows remained confined within the channel banks. This is likely because, in vegetated intertidal plains, both frictionally-dominated flow propagation and higher elevation of channel banks (relative to tidal excursions) ensure flow confinement and high in-channel velocities even for above-bankfull stages. In contrast, in unvegetated intertidal mudflats, similar flow resistance within and outside channels and lower elevation of channel banks produce widespread sheet flow at above-bankfull stages and limit in-channel velocities due to reduced flow confinement;

(2) Secondary currents appear to be mostly related to flood flows, and are generally stronger during overbank stages. In some cases, however, the orientation of secondary circulations is reversed compared to classic flow models in meander bends. Poorly-developed secondary circulations are observed at the bend apex. However, primary flow separation, coupled with localized flow measurements that did not include the entire channel cross-section, have likely limited our ability to detect secondary circulation cells during our field measurements.

(3) Field data collectively suggest limited control of curvature-induced helical flows on meander morphodynamics. This is most likely due to a consistent phase lag between maxima of primary (i.e., streamwise) and secondary (i.e., cross-sectional) velocities. Such a lag effectively limits the landward (seaward) transfer of secondary flows during the flood (ebb) phase, thus hampering the formation of coherent helical flow structures along the entire meander bends. These findings support the results of earlier studies that suggested that, in stark contrast with both river and salt-marsh meandering channels, meander morphodynamics in intertidal

mudflats are poorly related to bankfull hydrodynamics, in general, and curvature-induced helical flows in particular.

(4) We suggest that other morphodynamic processes drive the evolution of intertidal mudflat meander bends. Late-ebb tidal flows likely exert strong control on meander morphodynamics due to sustained velocities and pronounced seepage flows, which determine significant sediment transport as well as both bank undercutting and collapses. These effects are also possibly amplified by the absence of vegetation both within and outside the channel, as well as by significant bioturbation of the channel banks, which reduces bank resistance to erosion and enhances seepage flow. In addition, storm waves and both episodic and seasonal increases in discharges due to heavy rainfalls (e.g., related to the monsoon season) and melting snows can compound the morphological effects of late-ebb flows, producing abrupt morphologic changes and pronounced channel migration.

Additional field and modeling efforts would be required to corroborate the inferences presented in this study and to investigate how different tidal ranges and channel-bank elevations (relative to characteristic tidal oscillations) affect mudflat meander hydrodynamics and the related morphodynamic evolution. Particularly, cross-sectional measurements of tidal flow fields are needed to directly assess the scarce development of curvature-induced helical flows, whereas repeated measurement of flow fields during normal conditions and heavy rainfall events, coupled with morphological monitoring of channel bank evolution, would help clarify the relative importance of astronomic and meteorological forcings on the morphodynamics of intertidal mudflat meanders.

## Acknowledgments

This study was financially supported by the National Natural Science Foundation of China (U2240220, 41625021), the Innovation Program of Shanghai Municipal Education Commission (2019-01-07-00-05-E00027), the China Scholarship Council (CSC) scholarships (202106190084) and Jiangsu Special Program for Science and Technology Innovation (JSZRHYKJ2021006). We thank Zhenqiao Liu, Wei Feng, Jianxiong Sun, and Dongyun Wei for their help in field work. Special acknowledgments are given to Shibing Zhu for his help in grain size analysis.

## Open Research

The data sets generated and/or analyzed during the current study are freely available at https://doi.org/10.6084/m9.figshare.20161733.v2

## References


Azpiroz-Zabala, M., Cartigny, M. J. B., Sumner, E. J., Clare, M. A., Talling, P. J., Parsons, D. R., & Cooper, C. (2017). A General Model for the Helical Structure of Geophysical Flows in Channel Bends. *Geophysical Research Letters, 44*(23), 11,932-911,941. https://doi.org/10.1002/2017GL075721

Bathurst, J. C., Thorne, C. R., & Hey, R. D. (1977). Direct measurements of secondary currents in river bends. *Nature, 269*(5628), 504-506. https://doi.org/10.1038/269504a0

Bayliss-Smith, T. P., Healey, R., Lailey, R., Spencer, T., & Stoddart, D. R. (1979). Tidal flows in salt marsh creeks. *Estuarine and Coastal Marine Science, 9*(3), 235-255. https://doi.org/10.1016/0302-3524(79)90038-0

Bever, A. J., & MacWilliams, M. L. (2016). Factors influencing the calculation of periodic secondary circulation in a tidal river: numerical modelling of the lower Sacramento River, USA. *Hydrological processes, 30*(7), 995-1016. https://doi.org/10.1002/hyp.10690

Blanckaert, K. (2009). Saturation of curvature-induced secondary flow, energy losses, and turbulence in sharp open-channel bends: Laboratory experiments, analysis, and modeling. *Journal of Geophysical Research: Earth Surface, 114*(F3). https://doi.org/10.1029/2008JF001137

Blanckaert, K. (2011). Hydrodynamic processes in sharp meander bends and their morphological implications. *Journal of Geophysical Research: Earth Surface, 116*(F1). https://doi.org/10.1029/2010JF001806

Blanckaert, K., & de Vriend, H. J. (2003). Nonlinear modeling of mean flow redistribution in curved open channels. *Water Resources Research, 39*(12). https://doi.org/10.1029/2003WR002068

Blanckaert, K., Kleinhans, M. G., McLelland, S. J., Uijttewaal, W. S. J., Murphy, B. J., van de Kruijs, A., et al. (2013). Flow separation at the inner (convex) and outer (concave) banks of constant-width and widening open-channel bends. *Earth Surface Processes and Landforms, 38*(7), 696-716. https://doi.org/10.1002/esp.3324

Boon, J. D. (1975). Tidal discharge asymmetry in a salt marsh drainage system1,2. *Limnology and Oceanography, 20*(1), 71-80. https://doi.org/10.4319/lo.1975.20.1.0071

Bouma, T. J., Vries, M. B. D., Low, E., Kusters, L., Herman, P. M. J., Tánczos, I. C., et al. (2005). Flow hydrodynamics on a mudflat and in salt marsh vegetation: identifying general relationships for habitat characterisations. *Hydrobiologia, 540*(1-3), 259-274. https://doi.org/10.1007/s10750-004-7149-0

Bridge, J. S., & Jarvis, J. (1982). The dynamics of a river bend: a study in flow and sedimentary processes. *Sedimentology, 29*(4), 499-541. https://doi.org/10.1111/j.1365-3091.1982.tb01732.x

Brivio, L., Ghinassi, M., D'Alpaos, A., Finotello, A., Fontana, A., Roner, M., & Howes, N. (2016). Aggradation and lateral migration shaping geometry of a tidal point bar: An example from

874 salt marshes of the Northern Venice Lagoon (Italy). *Sedimentary Geology, 343*, 141-155.
875 https://doi.org/10.1016/j.sedgeo.2016.08.005
876 Brooks, H., Möller, I., Carr, S., Chirol, C., Christie, E., Evans, B., et al. (2021). Resistance of salt
877 marsh substrates to near-instantaneous hydrodynamic forcing. *Earth Surface Processes*
878 *and Landforms, 46*(1), 67-88. https://doi.org/10.1002/esp.4912
879 Chant, R. J. (2002). Secondary circulation in a region of flow curvature: Relationship with tidal
880 forcing and river discharge. *Journal of Geophysical Research, 107*(C9).
881 https://doi.org/10.1029/2001JC001082
882 Chen, J. D. (2016). *Sediment dynamic process on tidal flat under windy conditions.* (Master),
883 Nanjing University, Nanjing.
884 Chen, X., Zhang, C., H. Townend, I., Paterson, D. M., Gong, Z., Jiang, Q., et al. (2021). Biological
885 Cohesion as the Architect of Bed Movement Under Wave Action. *Geophysical Research*
886 *Letters, 48*(5), e2020GL092137. https://doi.org/10.1029/2020GL092137
887 Choi, K. (2010). Rhythmic Climbing-Ripple Cross-Lamination in Inclined Heterolithic
888 Stratification (IHS) of a Macrotidal Estuarine Channel, Gomso Bay, West Coast of Korea.
889 *Journal of Sedimentary Research, 80*(6), 550-561. https://doi.org/10.2110/jsr.2010.054
890 Choi, K. (2011). External controls on the architecture of inclined heterolithic stratification (IHS)
891 of macrotidal Sukmo Channel: Wave versus rainfall. *Marine Geology, 285*(1-4), 17-28.
892 https://doi.org/10.1016/j.margeo.2011.05.002
893 Choi, K. (2014). Morphology, sedimentology and stratigraphy of Korean tidal flats – Implications
894 for future coastal managements. *Ocean & Coastal Management, 102*, 437-448.
895 https://doi.org/10.1016/j.ocecoaman.2014.07.009
896 Choi, K., Hong, C. M., Kim, M. H., Oh, C. R., & Jung, J. H. (2013). Morphologic evolution of
897 macrotidal estuarine channels in Gomso Bay, west coast of Korea: Implications for the
898 architectural development of inclined heterolithic stratification. *Marine Geology, 346*, 343-
899 354. https://doi.org/10.1016/j.margeo.2013.10.005
900 Choi, K., & Jo, J. (2015). Morphodynamics of tidal channels In the Open Coast Macrotidal Flat,
901 Southern Ganghwa Island In Gyeonggi Bay, West Coast of Korea. *Journal of Sedimentary*
902 *Research, 85*(6), 582-595. https://doi.org/10.2110/jsr.2015.44
903 Christiansen, T., Wiberg, P. L., & Milligan, T. G. (2000). Flow and Sediment Transport on a Tidal
904 Salt Marsh Surface. *Estuarine, Coastal and Shelf Science, 50*(3), 315-331.
905 https://doi.org/10.1006/ecss.2000.0548
906 Coco, G., Zhou, Z., van Maanen, B., Olabarrieta, M., Tinoco, R., & Townend, I. (2013).
907 Morphodynamics of tidal networks: Advances and challenges. *Marine Geology, 346*, 1-16.
908 https://doi.org/10.1016/j.margeo.2013.08.005
909 Cosma, M., Finotello, A., Ielpi, A., Ventra, D., Oms, O., D'Alpaos, A., & Ghinassi, M. (2020).
910 Piracy-controlled geometry of tide-dominated point bars: Combined evidence from ancient
911 sedimentary successions and modern channel networks. *Geomorphology, 370*.
912 https://doi.org/10.1016/j.geomorph.2020.107402
913 Cosma, M., Lague, D., D'Alpaos, A., Leroux, J., Feldmann, B., & Ghinassi, M. (2022).
914 Sedimentology of a hypertidal point bar (Mont-Saint-Michel Bay, north-western France)
915 revealed by combining lidar time-series and sedimentary core data. *Sedimentology, 69*(3),
916 1179-1208. https://doi.org/10.1111/sed.12942
917 D'Alpaos, A., Lanzoni, S., Marani, M., Bonometto, A., Cecconi, G., & Rinaldo, A. (2007).
918 Spontaneous tidal network formation within a constructed salt marsh: Observations and

morphodynamic modelling. *Geomorphology, 91*(3-4), 186-197. https://doi.org/10.1016/j.geomorph.2007.04.013

D'Alpaos, A., Lanzoni, S., Marani, M., Fagherazzi, S., & Rinaldo, A. (2005). Tidal network ontogeny: Channel initiation and early development. *Journal of Geophysical Research-Earth Surface, 110*(F2). https://doi.org/10.1029/2004JF000182

D'Alpaos, A., Finotello, A., Goodwin, G. C. H., & Mudd, S. M. (2021). Salt Marsh Hydrodynamics. In *Salt Marshes* (pp. 53-81). https://doi.org/10.1017/9781316888933.005

Dietrich, W. E. (1987). Mechanics of flow and sediment transport in river bends. In K. S. Richards (Ed.), *River Channels: Environment and Process* (Vol. 18, pp. 179-227). Institute of British Geographers, Special Publication: Blackwell Oxford.

Dietrich, W. E., & Smith, J. D. (1983). Influence of the point bar on flow through curved channels. *Water Resources Research, 19*(5), 1173-1192. https://doi.org/10.1029/WR019i005p01173

Dinehart, R. L., & Burau, J. R. (2005). Averaged indicators of secondary flow in repeated acoustic Doppler current profiler crossings of bends. *Water Resources Research, 41*(9). https://doi.org/10.1029/2005WR004050

Engelund, F. (1974). Flow and Bed Topography in Channel Bends. *Journal of the Hydraulics Division, 100*(11), 1631-1648. https://doi.org/10.1061/JYCEAJ.0004109

Fagherazzi, S., Hannion, M., & D'Odorico, P. (2008). Geomorphic structure of tidal hydrodynamics in salt marsh creeks. *Water Resources Research, 44*(2). https://doi.org/10.1029/2007WR006289

Ferguson, R. I., Parsons, D. R., Lane, S. N., & Hardy, R. J. (2003). Flow in meander bends with recirculation at the inner bank. *Water Resources Research, 39*(11). https://doi.org/10.1029/2003WR001965

Finotello, A., Canestrelli, A., Carniello, L., Ghinassi, M., & D'Alpaos, A. (2019). Tidal flow asymmetry and discharge of lateral tributaries drive the evolution of a microtidal meander in the Venice Lagoon (Italy). *Journal of Geophysical Research: Earth Surface, 124*(12), 3043-3066. https://doi.org/10.1029/2019JF005193

Finotello, A., Capperucci, R. M., Bartholomä, A., D'Alpaos, A., & Ghinassi, M. (2022). Morpho-sedimentary evolution of a microtidal meandering channel driven by 130-years of natural and anthropogenic modifications of the Venice Lagoon (Italy). *Earth Surface Processes and Landforms, n/a*(n/a), 1-17. https://doi.org/10.1002/esp.5396

Finotello, A., D'Alpaos, A., Bogoni, M., Ghinassi, M., & Lanzoni, S. (2020). Remotely-sensed planform morphologies reveal fluvial and tidal nature of meandering channels. *Scientific Reports, 10*(1), 54. https://doi.org/10.1038/s41598-019-56992-w

Finotello, A., D'Alpaos, A., Lazarus, E. D., & Lanzoni, S. (2019). High curvatures drive river meandering: COMMENT. *Geology, 47*(10), e485. https://doi.org/10.1130/G46761C.1

Finotello, A., Ghinassi, M., Carniello, L., Belluco, E., Pivato, M., Tommasini, L., & D'Alpaos, A. (2020). Three‐Dimensional flow structures and morphodynamic evolution of microtidal meandering channels. *Water Resources Research, 56*(7). https://doi.org/10.1029/2020WR027822

Flemming, H.-C., & Wuertz, S. (2019). Bacteria and archaea on Earth and their abundance in biofilms. *Nature Reviews Microbiology, 17*(4), 247-260. https://doi.org/10.1038/s41579-019-0158-9

Folkard, A. M. (2005). Hydrodynamics of model Posidonia oceanica patches in shallow water. *Limnology and Oceanography, 50*(5), 1592-1600. https://doi.org/10.4319/lo.2005.50.5.1592

965 Friedman, G. M. (1962). Comparison of moment measures for sieving and thin-section data in
966 sedimentary petrological studies. *Journal of Sedimentary Research, 32*(1), 15-25.
967 https://doi.org/10.1306/74D70C36-2B21-11D7-8648000102C1865D
968 Friedrichs, C. T. (2011). Tidal Flat Morphodynamics: A Synthesis. In J. D. Hansom & B. W.
969 Fleming (Eds.), *Treatise on Estuarine and Coastal Science* (Vol. 3, pp. 137-170).
970 Amsterdam, Netherlands: Elsevier. https://doi.org/10.1016/B978-0-12-374711-2.00307-7
971 Friedrichs, C. T., & Aubrey, D. G. (1988). Non-linear tidal distortion in shallow well-mixed
972 estuaries: a synthesis. *Estuarine, Coastal and Shelf Science, 27*(5), 521-545.
973 https://doi.org/10.1016/0272-7714(88)90082-0
974 Friedrichs, C. T., & Perry, J. E. (2001). Tidal salt marsh morphodynamics: a synthesis. *Journal of*
975 *Coastal Research*, 7-37. https://www.jstor.org/stable/25736162
976 Frothingham, K. M., & Rhoads, B. L. (2003). Three-dimensional flow structure and channel
977 change in an asymmetrical compound meander loop, Embarras River, Illinois. *Earth*
978 *Surface Processes and Landforms, 28*(6), 625-644. https://doi.org/10.1002/esp.471
979 Gabet, E. J. (1998). Lateral Migration and Bank Erosion in a Saltmarsh Tidal Channel in San
980 Francisco Bay, California. *Estuaries, 21*(4). https://doi.org/10.2307/1353278
981 Gao, S. (2019). Geomorphology and Sedimentology of Tidal Flats. In *Coastal Wetlands* (pp. 359-
982 381): Elsevier. https://doi.org/10.1016/B978-0-444-63893-9.00010-1
983 Gardner, L. R., & Wilson, A. M. (2006). Comparison of four numerical models for simulating
984 seepage from salt marsh sediments. *Estuarine, Coastal and Shelf Science, 69*(3), 427-437.
985 https://doi.org/10.1016/j.ecss.2006.05.009
986 Geng, L., D'Alpaos, A., Sgarabotto, A., Gong, Z., & Lanzoni, S. (2021). Intertwined Eco-
987 Morphodynamic Evolution of Salt Marshes and Emerging Tidal Channel Networks. *Water*
988 *Resources Research, 57*(11), e2021WR030840. https://doi.org/10.1029/2021WR030840
989 Ghinassi, M., D'Alpaos, A., Tommasini, L., Brivio, L., Finotello, A., Stefani, C., & Walsh, J. P.
990 (2019). Tidal currents and wind waves controlling sediment distribution in a subtidal point
991 bar of the Venice Lagoon (Italy). *Sedimentology, 66*(7), 2926-2949.
992 https://doi.org/10.1111/sed.12616
993 Goring, D. G., & Nikora, V. I. (2002). Despiking acoustic Doppler velocimeter data. *Journal of*
994 *Hydraulic Engineering-Asce, 128*(1), 117-126. https://doi.org/10.1061/(Asce)0733-
995 9429(2002)128:1(117)
996 Guerra, M., & Thomson, J. (2017). Turbulence Measurements from Five-Beam Acoustic Doppler
997 Current Profilers. *Journal of Atmospheric and Oceanic Technology, 34*(6), 1267-1284.
998 https://doi.org/10.1175/JTECH-D-16-0148.1
999 Guimond, J., & Tamborski, J. (2021). Salt Marsh Hydrogeology: A Review. *Water, 13*(4), 543.
1000 https://doi.org/10.3390/w13040543
1001 Guo, L., Wang, Z. B., Townend, I., & He, Q. (2019). Quantification of Tidal Asymmetry and Its
1002 Nonstationary Variations. *Journal of Geophysical Research: Oceans, 124*(1), 773-787.
1003 https://doi.org/10.1029/2018JC014372
1004 Hackney, C., Best, J., Leyland, J., Darby, S. E., Parsons, D., Aalto, R., & Nicholas, A. (2015).
1005 Modulation of outer bank erosion by slump blocks: Disentangling the protective and
1006 destructive role of failed material on the three-dimensional flow structure. *Geophysical*
1007 *Research Letters, 42*(24), 10,663-610,670. https://doi.org/10.1002/2015GL066481
1008 Harvey, G. L., Henshaw, A. J., Brasington, J., & England, J. (2019). Burrowing Invasive Species:
1009 An Unquantified Erosion Risk at the Aquatic-Terrestrial Interface. *Reviews of Geophysics,*

*57*(3), 1018-1036. https://agupubs.onlinelibrary.wiley.com/doi/abs/10.1029/2018RG000635

Hickin, E. J. (1978). Meandering channels. In G. V. Middleton, M. J. Church, M. Coniglio, L. A. Hardie, & F. J. Longstaffe (Eds.), *Encyclopedia of Sediments and Sedimentary Rocks* (pp. 703-709). Dordrecht: Springer Netherlands. https://doi.org/10.1007/978-1-4020-3609-5_134

Hickin, E. J., & Nanson, G. C. (1975). The Character of Channel Migration on the Beatton River, Northeast British Columbia, Canada. *Geological Society of America Bulletin, 86*(4), 487-494. https://doi.org/10.1130/0016-7606(1975)86<487:TCOCMO>2.0.CO;2

Hooke, J. M. (2013). River Meandering. In J. Shroder & E. Wohl (Eds.), *Treatise on Geomorphology* (Vol. 9, pp. 260-288). San Diego, CA: Academic Press. https://doi.org/10.1016/B978-0-12-374739-6.00241-4

Horstman, E. M., Bryan, K. R., & Mullarney, J. C. (2021). Drag variations, tidal asymmetry and tidal range changes in a mangrove creek system. *Earth Surface Processes and Landforms, 46*(9), 1828-1846. https://doi.org/10.1002/esp.5124

Hughes, Z. J. (2012). Tidal Channels on Tidal Flats and Marshes. In R. A. Davis Jr & R. W. Dalrymple (Eds.), *Principles of Tidal Sedimentology* (pp. 269-300). Dordrecht: Springer Netherlands. https://doi.org/10.1007/978-94-007-0123-6_11

Ishimatsu, A., Hishida, Y., Takita, T., Kanda, T., Oikawa, S., Takeda, T., & Huat, K. K. (1998). Mudskippers store air in their burrows. *Nature, 391*(6664), 237-238. https://doi.org/10.1038/34560

Kearney, W. S., & Fagherazzi, S. (2016). Salt marsh vegetation promotes efficient tidal channel networks. *Nature Communications, 7*(1), 12287. https://doi.org/10.1038/ncomms12287

Kearney, W. S., Mariotti, G., Deegan, L. A., & Fagherazzi, S. (2017). Stage‐discharge relationship in tidal channels. *Limnology and Oceanography: Methods, 15*(4), 394-407. https://doi.org/10.1002/lom3.10168

Keevil, C. E., Parsons, D. R., Keevil, G. M., & Ainsley, M. (2015). Three-dimensional meander bend flow within the tidally influenced fluvial zone. In P. J. Ashworth, J. L. Best, & D. R. Parsons (Eds.), *Developments in Sedimentology* (Vol. 68, pp. 127-148): Elsevier. https://doi.org/10.1016/B978-0-444-63529-7.00006-7

Kim, S. C., Friedrichs, C. T., Maa, J. P. Y., & Wright, L. D. (2000). Estimating bottom stress in tidal boundary layer from acoustic Doppler velocimeter data. *Journal of Hydraulic Engineering, 126*(6), 399-406. https://doi.org/10.1061/(ASCE)0733-9429(2000)126:6(399)

Kirwan, M. L., & Megonigal, J. P. (2013). Tidal wetland stability in the face of human impacts and sea-level rise. *Nature, 504*(7478), 53-60. https://doi.org/10.1038/nature12856

Klein, G. d. (1985). Intertidal flats and intertidal sand bodies. In R. A. Davis (Ed.), *Coastal sedimentary environments* (pp. 187-224). New York: Springer. https://doi.org/10.1007/978-1-4612-5078-4_3

Kleinhans, M. G., Schuurman, F., Bakx, W., & Markies, H. (2009). Meandering channel dynamics in highly cohesive sediment on an intertidal mud flat in the Westerschelde estuary, the Netherlands. *Geomorphology, 105*(3-4), 261-276. https://doi.org/10.1016/j.geomorph.2008.10.005

Kranenburg, W. M., Geyer, W. R., Garcia, A. M. P., & Ralston, D. K. (2019). Reversed Lateral Circulation in a Sharp Estuarine Bend with Weak Stratification. *Journal of Physical Oceanography, 49*(6), 1619-1637. https://doi.org/10.1175/JPO-D-18-0175.1

Lan, T. F., Wu, H., Tang, J. P., Li, Z., & Wang, Y. P. (2019). A preliminary study on in situ bottom boundary layer measurement near the seabed of estuaries by using a novel high-frequency Acoustic Doppler Current Profiler (in Chinese). *Marine Science Bulletin, 38*(6), 640-649.

Lane, S. N., Bradbrook, K. F., Richards, K. S., Biron, P. M., & Roy, A. G. (2000). Secondary circulation cells in river channel confluences: measurement artefacts or coherent flow structures? *Hydrological processes, 14*(11-12), 2047-2071. https://doi.org/10.1002/1099-1085(20000815/30)14:11/12<2047::AID-HYP54>3.0.CO;2-4

Leeder, M. R., & Bridges, P. H. (1975). Flow separation in meander bends. *Nature, 253*(5490), 338-339. https://doi.org/10.1038/253338a0

Leite Ribeiro, M., Blanckaert, K., Roy, A. G., & Schleiss, A. J. (2012). Flow and sediment dynamics in channel confluences. *Journal of Geophysical Research: Earth Surface, 117*(F1). https://doi.org/10.1029/2011JF002171

Li, H. Q., Yin, Y., Shi, Y., He, C. H., & Liu, X. Y. (2011). Micro-morphology and contemporary sedimentation rate of tidal flat in Rudong, Jiangsu Province (in Chinese). *Journal of Palaeogeography, 13*(02), 150-160.

Liaghat, A., Mohammadi, K., & Rahmanshahi, M. (2014). 3D investigation of flow hydraulic in U shape meander bends with constant, decreasing and increasing width. *Journal of river engineering, 2*(3), 12-23.

Liu, Z. X., Huang, Y. C., & Zhang, Q. N. (1989). Tidal current ridges in the Southwestern Yellow Sea. *Journal of Sedimentary Petrology, Vol. 59*, 432-437. https://doi.org/10.1306/212F8FB7-2B24-11D7-8648000102C1865D

McLachlan, R. L., Ogston, A. S., Asp, N. E., Fricke, A. T., Nittrouer, C. A., & Gomes, V. J. C. (2020). Impacts of tidal-channel connectivity on transport asymmetry and sediment exchange with mangrove forests. *Estuarine, Coastal and Shelf Science, 233*, 106524. https://doi.org/10.1016/j.ecss.2019.106524

Morales, J. A. (2022). Tide-Dominated Systems II: Tidal Flats and Wetlands. In J. A. Morales (Ed.), *Coastal Geology* (pp. 289-307). Cham: Springer International Publishing. https://doi.org/10.1007/978-3-030-96121-3_20

Murray, N. J., Phinn, S. R., DeWitt, M., Ferrari, R., Johnston, R., Lyons, M. B., et al. (2019). The global distribution and trajectory of tidal flats. *Nature, 565*(7738), 222-225. https://doi.org/10.1038/s41586-018-0805-8

Murray, N. J., Worthington, T. A., Bunting, P., Duce, S., Hagger, V., Lovelock, C. E., et al. (2022). High-resolution mapping of losses and gains of Earth's tidal wetlands. *science, 376*(6594), 744-749. https://doi.org/10.1126/science.abm9583

Nidzieko, N. J., Hench, J. L., & Monismith, S. G. (2009). Lateral Circulation in Well-Mixed and Stratified Estuarine Flows with Curvature. *Journal of Physical Oceanography, 39*(4), 831-851. https://doi.org/10.1175/2008JPO4017.1

Parsons, D. R., Ferguson, R. I., Lane, S. N., & Hardy, R. J. (2004). Flow structures in meander bends with recirculation zones: implications for bend movements. In C. Greco & D. Morte (Eds.), *River Flow* (pp. 49-57). London: Taylor & Francis.

Parsons, D. R., Jackson, P. R., Czuba, J. A., Engel, F. L., Rhoads, B. L., Oberg, K. A., et al. (2013). Velocity Mapping Toolbox (VMT): a processing and visualization suite for moving-vessel ADCP measurements. *Earth Surface Processes and Landforms, 38*(11), 1244-1260. https://doi.org/10.1002/esp.3367

Passarelli, C., Hubas, C., & Paterson, D. M. (2018). Mudflat Ecosystem Engineers and Services. In P. G. Beninger (Ed.), *Mudflat Ecology* (pp. 243-269). Cham: Springer International Publishing. https://doi.org/10.1007/978-3-319-99194-8_10

Pein, J., Valle-Levinson, A., & Stanev, E. V. (2018). Secondary Circulation Asymmetry in a Meandering, Partially Stratified Estuary. *Journal of Geophysical Research: Oceans, 123*(3), 1670-1683. https://doi.org/10.1002/2016JC012623

Perillo, G. M. E., Minkoff, D. R., & Piccolo, M. C. (2005). Novel mechanism of stream formation in coastal wetlands by crab–fish–groundwater interaction. *Geo-Marine Letters, 25*(4), 214-220. https://doi.org/10.1007/s00367-005-0209-2

Pilkey, O. H., & Cooper, J. A. G. (2004). Society and sea level rise. *science, 303*(5665), 1781-1782. https://doi.org/10.1126/science.1093515

Prandtl, L. (1926). Bemerkung zu dem Aufsatz von A. Einstein: Die Ursache der Mäanderbildung und das sogenannte Baersche Gesetz. *Naturwissenschaften, 14*(26), 619-620. https://doi.org/10.1007/BF01507352

Ren, M. E., & Shi, Y. L. (1986). Sediment discharge of the Yellow River (China) and its effect on the sedimentation of the Bohai and the Yellow Sea. *Continental Shelf Research, 6*(6), 785-810. https://doi.org/10.1016/0278-4343(86)90037-3

Rhoads, B. L., & Kenworthy, S. T. (1995). Flow structure at an asymmetrical stream confluence. *Geomorphology, 11*(4), 273-293. https://doi.org/10.1016/0169-555X(94)00069-4

Rinaldo, A., Fagherazzi, S., Lanzoni, S., Marani, M., & Dietrich, W. E. (1999a). Tidal networks 2. Watershed delineation and comparative network morphology. *Water Resources Research, 35*(12), 3905-3917. https://doi.org/10.1029/1999WR900237

Rinaldo, A., Fagherazzi, S., Lanzoni, S., Marani, M., & Dietrich, W. E. (1999b). Tidal networks: 3. Landscape-forming discharges and studies in empirical geomorphic relationships. *Water Resources Research, 35*(12), 3919-3929. https://doi.org/10.1029/1999WR900238

Rogers, K., & Woodroffe, C. D. (2015). Tidal Flats and Salt Marshes. In *Coastal Environments and Global Change* (pp. 227-250). https://doi.org/10.1002/9781119117261.ch10

Rozovskiĭ, I. L. v. (1957). *Flow of water in bends of open channels (in Russian)*: Academy of Sciences of the Ukrainian SSR.

Schindfessel, L., Creëlle, S., & De Mulder, T. (2015). Flow Patterns in an Open Channel Confluence with Increasingly Dominant Tributary Inflow. *Water, 7*(9), 4724-4751. https://doi.org/10.3390/w7094724

Schwarz, C., van Rees, F., Xie, D., Kleinhans, M. G., & van Maanen, B. (2022). Salt marshes create more extensive channel networks than mangroves. *Nature Communications, 13*(1), 2017. https://doi.org/10.1038/s41467-022-29654-1

Sgarabotto, A., D'Alpaos, A., & Lanzoni, S. (2021). Effects of Vegetation, Sediment Supply and Sea Level Rise on the Morphodynamic Evolution of Tidal Channels. *Water Resources Research, 57*(7), e2020WR028577. https://doi.org/10.1029/2020WR028577

Shi, B., Wang, Y. P., Du, X., Cooper, J. R., Li, P., Li, M. L., & Yang, Y. (2016). Field and theoretical investigation of sediment mass fluxes on an accretional coastal mudflat. *Journal of Hydro-environment Research, 11*, 75-90. https://doi.org/10.1016/j.jher.2016.01.002

Shi, B., Wang, Y. P., Wang, L. H., Li, P., Gao, J., Xing, F., & Chen, J. D. (2018). Great differences in the critical erosion threshold between surface and subsurface sediments: A field investigation of an intertidal mudflat, Jiangsu, China. *Estuarine, Coastal and Shelf Science, 206*, 76-86. https://doi.org/10.1016/j.ecss.2016.11.008

1145 Sisulak, C. F., & Dashtgard, S. E. (2012). Seasonal Controls On the Development And Character
1146 of Inclined Heterolithic Stratification In A Tide-Influenced, Fluvially Dominated Channel:
1147 Fraser River, Canada. *Journal of Sedimentary Research, 82*(4), 244-257.
1148 https://doi.org/10.2110/jsr.2012.21
1149 Solari, L., Seminara, G., Lanzoni, S., Marani, M., & Rinaldo, A. (2002). Sand bars in tidal channels
1150 Part 2. Tidal meanders. *Journal of Fluid Mechanics, 451*, 203-238.
1151 https://doi.org/10.1017/S0022112001006565
1152 Somsook, K., Duka, M. A., Olap, N. A., Casila, J. C. C., & Yokoyama, K. (2020). Direct
1153 measurement of secondary circulation in a meandering macrotidal estuary. *Sci Total*
1154 *Environ, 739*, 139503. https://doi.org/10.1016/j.scitotenv.2020.139503
1155 Somsook, K., Olap, N. A., Duka, M. A., Veerapaga, N., Shintani, T., & Yokoyama, K. (2022).
1156 Analysis of interaction between morphology and flow structure in a meandering macro-
1157 tidal estuary using 3-D hydrodynamic modeling. *Estuarine, Coastal and Shelf Science, 264*.
1158 https://doi.org/10.1016/j.ecss.2021.107687
1159 Sullivan, J. C., Torres, R., Garrett, A., Blanton, J., Alexander, C., Robinson, M., et al. (2015).
1160 Complexity in salt marsh circulation for a semienclosed basin. *Journal of Geophysical*
1161 *Research: Earth Surface, 120*(10), 1973-1989. https://doi.org/10.1002/2014JF003365
1162 Temmerman, S., Meire, P., Bouma, T. J., Herman, P. M., Ysebaert, T., & De Vriend, H. J. (2013).
1163 Ecosystem-based coastal defence in the face of global change. *Nature, 504*(7478), 79-83.
1164 https://doi.org/10.1038/nature12859
1165 Termini, D., & Piraino, M. (2011). Experimental analysis of cross-sectional flow motion in a large
1166 amplitude meandering bend. *Earth Surface Processes and Landforms, 36*(2), 244-256.
1167 https://doi.org/10.1002/esp.2095
1168 Thorne, C. R., Zevenbergen, L. W., Pitlick, J. C., Rais, S., Bradley, J. B., & Julien, P. Y. (1985).
1169 Direct measurements of secondary currents in a meandering sand-bed river. *Nature,*
1170 *315*(6022), 746-747. https://doi.org/10.1038/315746a0
1171 Tu, J. B., Fan, D. D., Zhang, Y., & Voulgaris, G. (2019). Turbulence, Sediment‐Induced
1172 Stratification, and Mixing Under Macrotidal Estuarine Conditions (Qiantang Estuary,
1173 China). *Journal of Geophysical Research: Oceans, 124*(6), 4058-4077.
1174 https://doi.org/10.1029/2018JC014281
1175 van Maanen, B., Coco, G., & Bryan, K. R. (2015). On the ecogeomorphological feedbacks that
1176 control tidal channel network evolution in a sandy mangrove setting. *Proc Math Phys Eng*
1177 *Sci, 471*(2180), 20150115. https://doi.org/10.1098/rspa.2015.0115
1178 Vandenbruwaene, W., Schwarz, C., Bouma, T. J., Meire, P., & Temmerman, S. (2015).
1179 Landscape-scale flow patterns over a vegetated tidal marsh and an unvegetated tidal flat:
1180 Implications for the landform properties of the intertidal floodplain. *Geomorphology, 231*,
1181 40-52. https://doi.org/10.1016/j.geomorph.2014.11.020
1182 Voulgaris, G., & Meyers, S. T. (2004). Temporal variability of hydrodynamics, sediment
1183 concentration and sediment settling velocity in a tidal creek. *Continental Shelf Research,*
1184 *24*(15), 1659-1683. https://doi.org/10.1016/j.csr.2004.05.006
1185 Vousdoukas, M. I., Ranasinghe, R., Mentaschi, L., Plomaritis, T. A., Athanasiou, P., Luijendijk,
1186 A., & Feyen, L. (2020). Sandy coastlines under threat of erosion. *Nature Climate Change,*
1187 *10*(3), 260-263. https://doi.org/10.1038/s41558-020-0697-0
1188 Wang, X. Y., & Ke, X. K. (1997). Grain-size characteristics of the extant tidal flat sediments along
1189 the Jiangsu coast, China. *Sedimentary Geology, 112*(1-2), 105-122.
1190 https://doi.org/10.1016/S0037-0738(97)00026-2

Wang, Y., & Zhu, D. K. (1990). Tidal flats of China (in Chinsese). *Quaternary Sciences, 10*(4), 291-300.

Wang, Y. P., Gao, S., Jia, J. J., Thompson, C. E. L., Gao, J., & Yang, Y. (2012). Sediment transport over an accretional intertidal flat with influences of reclamation, Jiangsu coast, China. *Marine Geology, 291-294*, 147-161. https://doi.org/10.1016/j.margeo.2011.01.004

Wang, Y. P., Voulgaris, G., Li, Y., Yang, Y., Gao, J. H., Chen, J., & Gao, S. (2013). Sediment resuspension, flocculation, and settling in a macrotidal estuary. *Journal of Geophysical Research: Oceans, 118*(10), 5591-5608. https://doi.org/10.1002/jgrc.20340

Wang, Y. P., Zhang, R. S., & Gao, S. (1999a). Geomorphic and hydrodynamic responses in salt marsh-tidal creek systems, Jiangsu, China. *Chinese Science Bulletin, 44*(6), 544-549. https://doi.org/10.1007/BF02885545

Wang, Y. P., Zhang, R. S., & Gao, S. (1999b). Velocity variations in salt marsh creeks, Jiangsu, China. *Journal of Coastal Research, 15*(2), 471-477. http://www.jstor.org/stable/4298958

Wells, J. T., Adams, C. E., Park, Y.-A., & Frankenberg, E. W. (1990). Morphology, sedimentology and tidal channel processes on a high-tide-range mudflat, west coast of South Korea. *Marine Geology, 95*(2), 111-130. https://doi.org/10.1016/0025-3227(90)90044-K

Wilson, A. M., & Morris, J. T. (2012). The influence of tidal forcing on groundwater flow and nutrient exchange in a salt marsh-dominated estuary. *Biogeochemistry, 108*(1/3), 27-38. http://doi.org/10.1007/s10533-010-9570-y

Xin, P., Wilson, A., Shen, C., Ge, Z., Moffett, K. B., Santos, I. R., et al. (2022). Surface Water and Groundwater Interactions in Salt Marshes and Their Impact on Plant Ecology and Coastal Biogeochemistry. *Reviews of Geophysics, 60*(1), e2021RG000740. https://doi.org/10.1029/2021RG000740

Xing, F., Wang, Y. P., & Wang, H. V. (2012). Tidal hydrodynamics and fine-grained sediment transport on the radial sand ridge system in the southern Yellow Sea. *Marine Geology, 291-294*, 192-210. https://doi.org/10.1016/j.margeo.2011.06.006

Xu, M., Meng, K., Zhao, Y., & Zhao, L. (2019). Sedimentary Environment Evolution in East China's Coastal Tidal Flats: The North Jiangsu Radial Sand Ridges. *Journal of Coastal Research, 35*(3), 524-533. https://doi.org/10.2112/JCOASTRES-D-18-00006.1

Yang, S. L., Milliman, J. D., Xu, K. H., Deng, B., Zhang, X. Y., & Luo, X. X. (2014). Downstream sedimentary and geomorphic impacts of the Three Gorges Dam on the Yangtze River. *Earth-Science Reviews, 138*, 469-486. https://doi.org/10.1016/j.earscirev.2014.07.006

Zhao, K., Coco, G., Gong, Z., Darby, S. E., Lanzoni, S., Xu, F., et al. (2022). A Review on Bank Retreat: Mechanisms, Observations, and Modeling. *Reviews of Geophysics, 60*(2), e2021RG000761. https://doi.org/10.1029/2021RG000761

Zhao, K., Gong, Z., Xu, F., Zhou, Z., Zhang, C. K., Perillo, G. M. E., & Coco, G. (2019). The Role of Collapsed Bank Soil on Tidal Channel Evolution: A Process-Based Model Involving Bank Collapse and Sediment Dynamics. *Water Resources Research, 55*(11), 9051-9071. https://doi.org/10.1029/2019WR025514

Zhao, Y., Liu, Q., Huang, R., Pan, H., & Xu, M. (2020). Recent Evolution of Coastal Tidal Flats and the Impacts of Intensified Human Activities in the Modern Radial Sand Ridges, East China. *Int J Environ Res Public Health, 17*(9). https://doi.org/10.3390/ijerph17093191

Zhao, Y. Y., & Gao, S. (2015). Simulation of tidal flat sedimentation in response to typhoon—Induced storm surges: A case study from Rudong Coast, Jiangsu, China (in Chinsese). *Acta Sedimentologica Sinica, 33*(1), 79-90.

1236 Zhu, D. K., Ke, X., & Gao, S. (1986). Tidal flat sedimentation of Jiangsu coast (in Chinese). *J.*
1237 *Oceanogr. Huanghai Bohai Sea*, *4*(3), 19-27.
1238